Human coronaviruses disassemble processing bodies

Mariel Kleer[1,2,3*], Rory P. Mulloy[1,2,3*], Carolyn-Ann Robinson[1,2,3], Danyel Evseev[1,2,3], Maxwell P. Bui-Marinos[1,2,3], Elizabeth L. Castle[4], Arinjay Banerjee[5,6,7], Samira Mubareka[8,9], Karen Mossman[10,11] and Jennifer A. Corcoran[1,2,3 #]

[1]Microbiology, Immunology and Infectious Diseases Department, University of Calgary, Calgary, AB, Canada.
[2]Charbonneau Cancer Research Institute, University of Calgary, Calgary, AB, Canada.
[3]Snyder Institute for Chronic Diseases, University of Calgary, Calgary, AB, Canada.
[4]School of Biomedical Engineering, University of British Columbia, Vancouver, BC, Canada.
[5]Vaccine and Infectious Disease Organization, University of Saskatchewan; Saskatoon, SK, Canada
[6]Department of Veterinary Microbiology, Western College of Veterinary Medicine, University of Saskatchewan; Saskatoon, SK, Canada
[7]Department of Biology, University of Waterloo; Waterloo, ON, Canada
[8]Department of Laboratory Medicine and Pathobiology, University of Toronto, Toronto, ON, Canada
[9]Sunnybrook Research Institute, Toronto, ON, Canada
[10]Department of Medicine, Master University, Hamilton, ON, Canada
[11]Institute for Infectious Disease Research, McMaster University, Hamilton, ON, Canada

[*]Equal contribution
[#]Corresponding Author

Abstract

A dysregulated proinflammatory cytokine response is characteristic of severe coronavirus infections caused by SARS-CoV-2, yet our understanding of the underlying mechanism responsible for this imbalanced immune response remains incomplete. Processing bodies (PBs) are cytoplasmic membraneless ribonucleoprotein granules that control innate immune responses by mediating the constitutive decay or suppression of mRNA transcripts, including many that encode proinflammatory cytokines. PB formation promotes turnover or suppression of cytokine RNAs, whereas PB disassembly corresponds with the increased stability and/or translation of these cytokine RNAs. Many viruses cause PB disassembly, an event that can be viewed as a switch that rapidly relieves cytokine RNA repression and permits the infected cell to respond to viral infection. Prior to this report, no information was known about how human coronaviruses (hu CoVs) impacted PBs. Here, we show SARS-CoV-2 and the common cold hu CoVs, OC43 and 229E, induced PB loss. We screened a SARS-CoV-2 gene library and identified that expression of the viral nucleocapsid (N) protein from SARS-CoV-2 was sufficient to mediate PB disassembly. RNA fluorescent *in situ* hybridization revealed that N protein-mediated PB loss correlated with elevated RNA for PB-localized transcripts encoding TNF and IL-6. Ectopic expression of the N proteins from five other human coronaviruses (OC43, MERS, 229E, NL63 and SARS-CoV-1) did not cause significant PB disassembly, suggesting that this feature is unique to SARS-CoV-2 N protein. These data suggest that SARS-CoV-2-mediated PB disassembly contributes to enhanced proinflammatory cytokine production observed during severe SARS-CoV-2 infection.

60 **Introduction**

61 Processing bodies (PBs) are membraneless ribonucleoprotein (RNP) granules found in the
62 cytoplasm of all cells [1,2] . PBs control cellular gene expression because they either degrade or
63 sequester cellular RNA transcripts, preventing their translation into protein. PBs contain many
64 enzymes required for mRNA turnover, including those needed for decapping (Dcp2 and co-
65 factors Dcp1a and Edc4/Hedls) and decay of the RNA body (5'-3' exonuclease Xrn1 and RNA
66 helicase Rck/DDX6) and some components of the RNA-induced silencing complex [3,4]. Not all
67 coding RNAs are regulated by PBs, but those that are typically encode potent regulatory
68 molecules like growth factors, pro-inflammatory cytokines, and angiogenic factors. One group of
69 protein-coding mRNAs commonly found in PBs bear destabilizing AU-rich elements (AREs) in
70 their 3'-untranslated regions (3'-UTRs) and include most proinflammatory cytokine transcripts
71 [5-7]. These RNAs shuttle to PBs by virtue of interactions between the AU-rich element and
72 RNA-binding proteins (RBPs) [3,8-11]. We and others showed that the presence of PBs
73 correlates with increased turnover/suppression of ARE-mRNAs [7,12-15] . Conversely, when
74 PBs are lost, constitutive ARE-mRNA suppression is reversed, and ARE-mRNA transcripts
75 and/or their translation products accumulate. Therefore, PB disassembly can be viewed as a
76 switch that permits cells to rapidly respond and translate ARE-containing proinflammatory
77 cytokine RNA into molecules such as IL-6, IL-8, IL-1β, and TNF [5]. PBs provide an extra layer
78 of post-transcriptional control enabling the cell to fine tune the production of potent molecules
79 like proinflammatory cytokines.

80

81 Although PBs are constitutive, they are also dynamic, changing in size and number in response
82 to different stimuli or stressors. This dynamic disassembly/assembly is possible because PBs
83 behave as biomolecular condensates that form via liquid-liquid phase separation of proteins [16-

84 19]. PBs form via sequential multivalent RNA-protein interactions, with a small group of
85 proteins that contain regions of intrinsic disorder serving as the essential scaffold onto which
86 additional proteins or RNA can be recruited as the PB matures [9,16,20-24]. Despite the
87 recognition of PBs as dynamic entities, our understanding of the signals that induce PB
88 disassembly remains incomplete. We and others have shown that stressors which activate the
89 p38/MK2 MAP kinase pathway, as well as many virus infections elicit PB disassembly
90 [12,13,15,25,26]. Disassembly can occur by a direct interaction between a viral protein(s) and a
91 PB component that is subsequently re-localized to viral replication and transcription
92 compartments (vRTCs) [27-29] or cleaved by viral proteases [30-32]. Viruses can also cause PB
93 disassembly indirectly by activating p38/MK2 signaling [12,13,26] .
94
95 There are numerous reports of viral gene products that trigger PB disassembly, yet corresponding
96 reports of viral gene products that stimulate PB formation are rare, suggesting that PBs possess
97 direct antiviral function and their disassembly may favour viral replication in ways that we do
98 not yet grasp [33,34]. Even though other RNPs, such as stress granules, have emerged as
99 important components of our antiviral defenses that contribute to sensing virus and triggering
100 innate immune responses, evidence to support a direct antiviral role for PBs is less well
101 established [34-37] . A direct-acting antiviral role has been defined for several PB-localized
102 enzymes that impede viral replication (e.g. APOBEC3G, MOV10). However, in these cases, the
103 mechanism of viral restriction was attributed to the enzymatic activity of the PB protein(s)
104 whereas its localization to PBs was not deemed as significant [28,29,31,38-45]. Nonetheless, the
105 disassembly of PBs by diverse viruses strongly suggests they negatively regulate virus
106 replication. The reason viruses disassemble PBs may be to limit their antiviral activity; however,

107 because PBs also control turnover/suppression of many proinflammatory cytokine transcripts,
108 their disruption by viruses contributes to high proinflammatory cytokine levels, alerting immune
109 cells to the infection.
110
111 The family *Coronaviridae* includes seven viruses that infect humans, including the four
112 circulating 'common cold' coronaviruses (CoVs), CoV-OC43, CoV-229E, CoV-NL63, and
113 CoV-HKU1 and three highly pathogenic viruses that cause severe disease in humans: MERS-
114 CoV, SARS-CoV, and the recently emerged SARS-CoV-2 [46-51] . Severe COVID-19 is
115 characterized by aberrant proinflammatory cytokine production, endothelial cell (EC)
116 dysfunction and multiple organ involvement [52-64] . Even with intense study, we do not yet
117 appreciate precisely how SARS-CoV-2 infection causes severe COVID-19 in some patients and
118 mild disease in others though a mismanaged or delayed IFN response and an overactive cytokine
119 response is thought to underlie severe outcomes [65-70] . Despite some contrasting reports, [71-
120 73], what is clear is that SARS-CoV-2 proteins use a multitude of mechanisms to outcompete
121 cellular antiviral responses [68,74-85].
122
123 To determine if SARS-CoV-2 and other CoVs interact with PBs to alter the cellular antiviral
124 response, we performed an analysis of PBs after CoV infection. Prior to this research, no
125 published literature was available on human CoVs and PBs, and only two previous reports
126 mentioned PB dynamics after CoV infection. Murine hepatitis virus (MHV) was reported to
127 increase PBs at early infection times, while transmissible gastroenteritis coronavirus (TGEV)
128 infected cells displayed complete PB loss by 16 hours post infection [86,87]. Observations that
129 SARS-CoV-2 infection induced elevated levels of many PB-regulated cytokines, such as IL-6,

130 IL-10, IL-1β and TNF [53,54,57,69,70] suggested that human CoVs like SARS-CoV-2 may
131 reshape the cellular innate immune response in part by targeting PBs for disassembly. We now
132 present the first evidence to show that three human CoVs, including SARS-CoV-2 trigger PB
133 disassembly during infection. By screening a SARS-CoV-2 gene library, we identified that the
134 nucleocapsid (N) protein was sufficient for PB disassembly. However, this feature is not
135 common for all human coronavirus N proteins, as overexpression of MERS-CoV-N, OC43-N,
136 229E-N and NL63-N was insufficient to induce PB loss and expression of SARS-CoV-1 N
137 protein displayed an intermediate phenotype. SARS-CoV-2 N protein expression was also
138 sufficient to increase levels of inflammatory transcripts that localize to PBs and are known to be
139 elevated during SARS-CoV-2 infection: IL-6 and TNF. Taken together, these results show that
140 PBs are targeted for disassembly by human CoV infection, and that this phenotype may
141 contribute in part to reshaping cytokine responses to SARS-CoV-2 infection.

142 **Results**

143 Infection with human coronaviruses causes PB loss

144 Endothelial cells (ECs) have emerged as playing a significant role in severe COVID; as sentinel
145 immune cells they are important sources for many of the cytokines elevated in severe disease and
146 are infected by SARS-CoV-2 *in vivo* [56,58-60,88]. However, others have shown that
147 commercial primary human umbilical vein endothelial cells (HUVECs) require ectopic
148 expression of the viral receptor, ACE2, to be susceptible to SARS-CoV-2 [89]. We recapitulated
149 those findings and showed that after HUVECs were transduced with an ACE2-expressing
150 lentivirus ($HUVEC^{ACE2}$), they were permissive for SARS-CoV-2 (Wuhan-like ancestral Toronto
151 isolate; TO-1) [90] (Fig S1A). To use $HUVEC^{ACE2}$ for studies on PB dynamics, we confirmed
152 that ACE2 ectopic expression had no effect on PB number in HUVECs (Fig S1B). Confirming
153 this, we infected $HUVEC^{ACE2}$ with SARS-CoV-2 (MOI=3) to determine if PBs were altered.
154 SARS-CoV-2 infected cells were identified by immunostaining for the viral nucleocapsid (N)
155 while PBs were identified by immunostaining for two different PB resident proteins, the RNA
156 helicase DDX6, and the decapping cofactor, Hedls. PBs, measured by staining for both markers,
157 were absent in most SARS-CoV-2 infected $HUVECs^{ACE2}$ by 24 hours post infection (Fig 1A-D).
158 We quantified the loss of cytoplasmic puncta using a method described previously [91] and
159 showed that by 24 hours post infection, SARS-CoV-2 infected cells displayed a significant
160 reduction in PBs compared to mock-infected controls (Fig 1B, D).

161

162 To confirm that PBs were reduced by SARS-CoV-2 infection of naturally permissive cells
163 derived from respiratory epithelium, we infected Calu-3 cells with SARS-CoV-2. Infected cells
164 were identified by immunostaining for N protein 24 hours after infection and PBs were stained

165 for DDX6 and Hedls. We observed PB loss in most but not all infected cells (Fig 1E-H). We
166 quantified PB loss and showed that by 24 hours post infection, SARS-CoV-2 infected Calu-3
167 cells also displayed a significant reduction in PBs compared to mock-infected controls (Fig F,
168 H). As the SARS-CoV-2 pandemic has progressed, new variants of concern (VOCs) have
169 continued to emerge [92,93]. To determine if VOCs also induced PB disassembly, we infected
170 $HUVEC^{ACE2}$ with SARS-CoV-2 VOCs Alpha, Beta, Gamma and Delta (MOI=2) and compared
171 PB disassembly to an ancestral isolate of SARS-CoV-2 (Wuhan-like Toronto isolate; TO-1) (Fig
172 2). Infected cells were identified by immunostaining for N protein 24 hours after infection and
173 PBs were identified using Hedls. Significant PB disassembly was observed for all VOCs,
174 although we noted slightly less PB disassembly mediated by TO-1 compared to the experiments
175 in Fig 1, likely due to the decrease in MOI between these two experiments (Fig 2).
176
177 To determine if PBs were lost in response to infection with other human coronaviruses, we
178 established infection models for the *Betacoronavirus*, OC43, and the *Alphacoronavirus*, 229E.
179 We found HUVECs were permissive to both OC43 and 229E (Fig S2A-B). We then performed a
180 time-course experiment wherein OC43-infected HUVECs were fixed at various times post
181 infection and immunostained for the viral N protein and the PB-resident protein DDX6. We
182 observed that PBs were largely absent in OC43 N protein-positive cells but present in mock-
183 infected control cells (Fig 3A-B). 229E-infected HUVECs were stained for DDX6 to measure
184 PBs and for dsRNA to denote infected cells due to a lack of commercially available antibodies
185 for 229E. CoV infected cells are known to form an abundance of dsRNA due to viral replication
186 and transcription from a positive-sense RNA genome making this a suitable marker for virally
187 infected cells [94] . In parallel, we confirmed 229E infection by performing RT-qPCR for viral

188 genomic and subgenomic RNA (Fig S2C-D). After 229E infection, we also found that PBs were
189 significantly reduced (Fig 3C-D). Because of antibody incompatibility, we were unable to co-
190 stain infected cells for the PB protein Hedls and OC43 N protein or dsRNA. In lieu of this, we
191 performed additional OC43 and 229E infections and co-stained infected cells using antibodies
192 for Hedls and DDX6 (Fig S3). We then performed additional quantification of PB loss using the
193 Hedls marker to label PBs. These data also show robust PB loss in response to infection with
194 OC43 and 229E (Fig S3).
195
196 PBs will disassemble if key scaffolding proteins are lost; these include the RNA helicase DDX6,
197 the translation suppressor 4E-T, the decapping cofactors Hedls/EDC4 and DCP1A, and the
198 scaffolding molecule Lsm14A [95] . To elucidate if CoV-infected cells displayed decreased
199 steady-state levels of PB resident proteins, we immunoblotted infected cell lysates for PB
200 proteins XRN1, DCP1A, or DDX6, and Hedls (Fig 4) and quantified protein levels by
201 densitometry (Fig S4). SARS-CoV-2 infection of $HUVEC^{ACE2}$ cells did not alter steady-state
202 levels of these proteins compared to uninfected cells (Fig 4A). OC43-infected HUVECs
203 displayed comparable levels of XRN1, DCP1A, and Hedls relative to uninfected cells; however,
204 OC43 infection decreased steady-state levels of DDX6 at both 12 hpi but not significantly at 24
205 hpi (Fig 4B). 229E-infected HUVECs showed no detectible change in PB protein expression
206 after infection compared to controls (Fig 4C).
207
208 PBs are important sites for the post-transcriptional control of inflammatory cytokine transcripts
209 containing AU-rich elements, and PB loss correlates with enhanced levels of some of these
210 transcripts [7,12-15]. To determine if ARE-mRNAs are elevated, and therefore subject to

211 regulation during CoV infection, we harvested total RNA from SARS-CoV-2-, OC43- or 229E-
212 infected HUVECs and performed RT-qPCR for five ARE-containing cytokine transcripts, IL-6,
213 CXCL8, COX-2, GM-CSF, and IL-1β (Fig 5A-C). Although we attempted to quantify TNF
214 RNA as well, but the low copy number (high Ct value) of TNF RNA in mock control samples
215 made quantification by RT-qPCR inaccurate and we were unable to measure the fold-increase of
216 TNF RNA after CoV infection. We observed increased levels of three ARE-containing
217 transcripts, IL-6, CXCL8, and COX-2, compared to uninfected cells, particularly in SARS-CoV-
218 2 infected cells (Fig 5A). Taken together, these data indicate that infection with human
219 coronaviruses including SARS-CoV-2 induces PB loss, and that some PB-regulated cytokine
220 ARE-mRNAs are elevated during CoV infection.
221
222 A screen of SARS-CoV-2 genes reveals mediators of PB loss
223 The genome of SARS-CoV-2 is predicted to contain up to 14 open reading frames (ORFs). The
224 two N-terminal ORFs (1a and 1ab) encode two large polyproteins which are processed by viral
225 proteases into 16 non-structural proteins (nsp1-16) essential for viral genome replication and
226 transcription [46] . The 3' end of the SARS-CoV-2 genome is predicted to code for ORFs that
227 are expressed from 9 subgenomic mRNAs [96]. Among these are the four structural proteins
228 spike (S), envelope (E), membrane (M) and nucleocapsid (N) and up to 9 potential accessory
229 proteins, not all of which have been validated as expressed in infected cells [96] . To test which
230 SARS-CoV-2 gene product(s) was responsible for PB disassembly, we obtained a plasmid
231 library of 27 SARS-CoV-2 genes from the Krogan lab; this library included 14 nsps (excluding
232 nsp3 and nsp16), all structural (S, E, M, N) and candidate accessory genes (ORFs 3a, 3b, 6, 7a,
233 7b, 8, 9b, 9c, 10) [96]. We individually transfected each plasmid and immunostained for each of

234 the SARS-CoV-2 proteins using antibodies to the Strep-tag II and for PBs using anti-DDX6 (Fig
235 6A, S5). Relative to control cells, many SARS-CoV-2 ORF transfected cells still displayed
236 DDX6-positive PBs; however, expression of some SARS-CoV-2 genes reduced DDX6-positive
237 puncta, including N and ORF7b (Fig 6A) to a similar or greater extent than our positive control,
238 the KapB protein from Kaposi's sarcoma-associated herpesvirus which we have previously
239 shown causes PB disassembly (Fig 6B, C) [13,91,97,98]. We quantified the number of DDX6-
240 positive PBs per cell for each transfection as in [91] and found that the average number of PBs
241 per cell was reduced relative to our negative control after transfection of eight SARS-CoV-2
242 genes: nsp7, ORF7b, N, ORF9b, ORF3b, nsp6, nsp1, and nsp11 (Fig 6D-E). This quantification
243 was performed in two different ways. In most cases, transfected cells were identified by co-
244 staining for the Strep-tag II fused to each gene (Fig 6A, S5). In such cases, we quantified DDX6-
245 positive puncta only in those cells that were transfected and not in bystander cells (Fig 6D,
246 thresholded). These data identified three SARS-CoV-2 proteins that may cause PB loss in a cell
247 autonomous manner: nsp7, ORF7b and N (Fig 6D). For the remaining transfections (nsp1, nsp5,
248 nsp6, nsp11, nsp13, nsp14, ORF3b, ORF6, ORF9b, ORF9c) immunostaining for the Strep-tag II
249 was not robust and we were unable to threshold our PB counts (Fig S5). In these samples, we
250 quantified PBs in all cells of the monolayer (Fig 6E, unthresholded). These data identified five
251 additional SARS-CoV-2 proteins from our screen that may cause PB loss: ORF9b, ORF3b, nsp1,
252 nsp6 and nsp11 (Fig 6E). We verified the expression of all constructs, including low expressors
253 (nsp1, nsp5, nsp6, nsp11, nsp13, nsp14, ORF3b, ORF6, ORF9b and ORF9c) by immunoblotting
254 whole cell lysates harvested from parallel transfections (Fig 6F). We were unable to detect nsp4,
255 ORF9c or ORF10 by immunoblotting; however, we did visualize expression of these proteins by
256 immunostaining (Fig 6F, S5). We eliminated low confidence hits (nsp7, ORF9b) and low

257 expressors (nsp6, nsp11) from further studies and proceeded with validation of the top four hits
258 (ORF7b, N, ORF3b, nsp1).
259
260 The nucleocapsid protein of SARS-CoV-2 induces PB disassembly
261 We tested four top hits from our PB screen in more relevant endothelial cells as these cells can
262 be infected, express inflammatory cytokines, and stain robustly for PBs. HUVECs were
263 transduced with recombinant lentiviruses expressing N, nsp1, ORF3b, and ORF7b or empty
264 vector control lentiviruses. We also included recombinant lentiviruses expressing nsp14 in this
265 experiment because of its exoribonuclease activity and ability to diminish cellular translation and
266 interferon responses [84]. Transduced cells were selected for transgene expression and then fixed
267 and stained for the endogenous PB marker protein DDX6 and for the Strep-tag II on each of
268 SARS-CoV-2 constructs. We observed robust staining of the viral nucleocapsid (N) protein in
269 the transduced cell population (Fig 7A) but were unable to detect expression of nsp1, nsp14,
270 ORF3b or ORF7b by immunostaining (Fig S6A). We quantified PB loss in the selected cells and
271 observed decreased PB numbers in cell populations expressing N, nsp14, ORF3b and ORF7b;
272 however, the most robust PB loss was induced in N-expressing cells, which displayed a
273 significant reduction in PB numbers as well as strong immunostaining (Fig 7B, Fig S6). We were
274 concerned that we could not detect the other four transgenes by immunostaining; therefore, we
275 performed immunoblotting for the Strep-II tag on lysates from each transduced cell population
276 (Fig S6C). Although we detected a strong band of ~50 kDa at the predicted molecular weight for
277 N, we were unable to detect bands for nsp14, ORF3b and ORF7b, while the most prominent
278 band for nsp1 did not migrate at the predicted molecular weight of ~20 kDa (Fig S6) [99,100] .
279 For these reasons, we decided to focus the remainder of our analysis on the N protein.

280

281 As PBs are dynamic RNP granules that undergo transient disassembly and assembly under basal
282 conditions, we wanted to determine whether N-mediated PB loss was caused by enhanced
283 disassembly of PBs or the prevention of PB *de novo* assembly. To determine this, we treated N-
284 expressing HUVECs with sodium arsenite, a known inducer of PB assembly [101] and
285 immunostained PBs for two different PB resident proteins, DDX6 and Hedls. Consistent with
286 our previous observation, PB loss was observed after N expression in our untreated control (Fig
287 7C-F). However, in N-expressing cells treated with sodium arsenite, PB formation could still be
288 observed, and was in fact increased, although the significance of this is unclear at present (Fig
289 7C-F). This means that N protein expression does not prevent PB formation, but instead triggers
290 PB disassembly, which can be reversed after an appropriate stimulus. These data showed that N
291 expression is sufficient to cause PB loss, and that the absence of PBs in N-expressing cells is a
292 result of enhanced PB disassembly not a block in PB formation.

293

294 We showed that human CoVs OC43 and 229E also cause PB loss during infection (Fig 3);
295 therefore, we were interested to determine if ectopic expression of nucleocapsid proteins from
296 these or other human CoVs were sufficient to mediate PB disassembly. To test this, we
297 transduced HUVECs with recombinant lentiviruses expressing the N protein from SARS-CoV-2
298 as well as N derived from Betacoronaviruses, MERS-CoV N-Flag and OC43 N. Expression of
299 MERS-CoV and OC43 N proteins did not lead to significant PB loss compared to SARS-CoV-2-
300 N (Fig 8A-B). We also tested two N proteins from human Alphacoronaviruses, 229E N-Flag and
301 NL63 N-Flag. 229E N protein failed to induce significant PB loss compared to SARS-CoV-2 N,
302 while unexpectedly, it appeared the expression of NL63 N protein increased PB numbers (Fig

303 8C-D). The significance of this increase is not yet clear. We also expressed the N protein from
304 the more closely related Betacoronavirus, SARS-CoV-1, and observed SARS-CoV-1 N protein
305 caused moderate PB loss, yet SARS-CoV-1 N protein-induced PB disassembly was not deemed
306 significant by statistical analysis (Fig 8E-F). We collected protein lysates in parallel and
307 performed immunoblotting to detect each CoV N protein (Fig 8G-I). We noted that CoV N
308 proteins are not expressed equally, thus, we cannot fully discount expression level as the reason
309 for the discrepancy in PB disassembly. This may be especially important for our analysis of
310 SARS-CoV-1 N protein, which showed an intermediate but non-significant PB disassembly
311 phenotype but was expressed at a lower level that SARS-CoV-2 N protein (Fig 8I).
312 Immunoblotting of steady state levels of PB resident proteins after N protein overexpression
313 showed that most PB proteins tested remained unchanged in the context of ectopic expression
314 (Fig 8G-I, Fig S7A). The exception to this was the decapping factor, Hedls/EDC4, which was
315 decreased after expression of SARS-CoV-2 N in one set of experiments but not in others, but
316 increased after expression of N proteins from MERS and OC43 (Fig 8G-I, Fig S7A). The
317 significance of this observation is also unclear.
318
319 To understand if PB disassembly correlates with changes to PB-regulated inflammatory cytokine
320 transcripts in our system, we performed immunofluorescence-RNA fluorescent *in situ*
321 hybridization (IF-FISH) to confirm the localization of inflammatory RNAs to PB foci. RNA
322 FISH was performed for two PB-regulated cytokine transcripts that contain AREs, those
323 encoding IL-6 and TNF, and for the GAPDH RNA, which does not contain AREs and is not
324 expected to localize to PBs [3]. To achieve a better signal-to-noise ratio for detection, we used
325 TNF to induce their transcription of IL-6 and TNF, which are lowly expressed in untreated cells.

326 First, we confirmed that TNF treatment alone did not significantly alter PB dynamics (Fig S8).
327 We then stained PBs using our antibody to Hedls and co-stained with probes that bound
328 GAPDH, TNF and IL-6 RNA transcripts. We repeatedly observed co-localization of both IL-6
329 and TNF RNA with PBs; in contrast, we observed extremely limited GAPDH co-localization
330 with PBs (Fig 9A). IL-6 and TNF transcripts were also present at much lower levels than
331 GAPDH RNA, consistent with the notion that ARE-containing transcripts are kept low by tight
332 transcriptional control and constitutive decay in PBs [14]. We then stained N protein-transduced
333 cells using our probes (Fig 9B). As expected, N protein expression induced loss of Hedls-
334 positive PB foci (not shown). In N-expressing cells, the signal for IL-6 and TNF RNA
335 redistributed from PB foci to the cytoplasm, and the probe intensity for both IL-6 and TNF was
336 markedly increased compared to control cells which lacked N protein (Fig 9B). We quantified
337 the change in FISH probe signal intensity per cell (Fig 9C). Compared to controls, N protein-
338 expressing cells displayed strongly increased TNF probe signal intensity and increased IL-6
339 probe signal intensity, whereas GAPDH probe signal intensity was not increased (Fig 9C). These
340 data support our hypothesis that PBs directly regulate proinflammatory cytokine transcripts and
341 that these PB-regulated mRNAs increase upon PB disassembly.
342
343 We then asked if N protein from SARS-CoV-2 or other human CoVs would increase ARE-RNA
344 transcript levels by RT-qPCR. We analyzed IL-6 and TNF transcript level, as well as two other
345 ARE-containing RNAs, encoding CXCL8 and COX-2 which were elevated after infection with
346 SARS-CoV-2 and OC43 (Fig 5). In uninduced ECs, the transcription of these mRNAs is
347 minimal; for example, TNF mRNA could not be readily detected by RT-qPCR without
348 transcriptional activation. Therefore, we treated control and N-expressing HUVECs with TNF to

349 activate cytokine transcription and then assessed if N protein expression enhanced cytokine
350 mRNA level post-transcriptionally. In the absence of TNF, no change of mRNA abundance was
351 observed for any of the coronaviruses N proteins tested (Fig 10A-C, 0 hour no treatment).
352 Ectopic expression of SARS-CoV-2 N enhanced transcript levels of IL-6, CXCL8, and TNF 24
353 hours after transcription was induced; however, this enhancement was not deemed significant by
354 statistical analysis (Fig 10A-C). In contrast, we did not observe any increase in transcript levels
355 after expression of N protein from MERS-CoV, OC43, 229E, or NL63 (Fig 10A-C), consistent
356 with earlier observations that their expression does not induce PB loss.
357
358 Taken together, we present the novel finding that three human CoVs induce PB loss and that for
359 SARS-CoV-2, the nucleocapsid protein is responsible for this loss. Moreover, we tested five
360 other human CoV N proteins and found that of these, only SARS-CoV-2 N was sufficient to
361 induce significant PB disassembly and concomitantly redistributed and enhanced levels of two
362 PB-localized cytokine mRNAs.
363

364 **Discussion**

365 In this manuscript, we present the first evidence to show that human CoVs, including SARS-
366 CoV-2, induce PB loss after infection. PBs are fundamental sites of post-transcriptional control
367 of gene expression and are particularly relevant to the regulation of cytokine production. Our
368 major findings are as follows: i) Three human coronaviruses, SARS-CoV-2, OC43, and 229E
369 induced PB loss. ii) The SARS-CoV-2 nucleocapsid (N) protein was sufficient to cause PB loss.
370 iii) N protein expression elevated levels of PB-localized cytokine transcripts encoding IL-6 and
371 TNF. Taken together, these data point to PB loss as a feature of SARS-CoV-2 infection.
372 Moreover, because viral induced PB disassembly elevates some PB-regulated cytokine
373 transcripts, this phenotype may contribute to the dysregulation of proinflammatory molecules
374 observed in severe SARS-CoV-2 infection.
375
376 We screened 27 SARS-CoV-2 gene products by transfection in HeLa cells [96] and initially
377 identified eight candidate genes that reduced PB numbers (Fig 6). Validation of a subset of these
378 in HUVECs revealed that the most robust and consistent mediator of PB loss was the SARS-
379 CoV-2 viral N protein (Fig 7). The N protein is the most abundant produced protein during CoV
380 replication [102]. The SARS-CoV-2 N protein is 419 amino acids long and has two globular and
381 three intrinsically disordered protein domains, including a central disordered serine-arginine
382 (SR-rich) linker region [102-104]. The N protein is a multifunctional RNA-binding protein
383 (RBP) essential for viral replication; it coats the viral genome and promotes viral particle
384 assembly [46,104-107]. Several recent reports have shown that N protein undergoes liquid-liquid
385 phase separation with RNA, an event which may be regulated by phosphorylation of multiple
386 serine residues in the SR-region and is an important feature of viral assembly [107-112] . The N

387 protein is also an important modulator of antiviral responses [85,113,114]. A recent study
388 showed that low doses of N protein supressed the production of IFN and some PB-regulated
389 inflammatory cytokines, while high doses of N protein promoted their production [85] . These
390 observations are consistent with our phenotype of PB disassembly, which correlates with later
391 infection times, high expression of N protein and immunofluorescent staining throughout the
392 cytoplasm (Fig 1, Fig 7).
393
394 We subsequently screened five other coronavirus N proteins from OC43, MERS, 229E, NL63,
395 and SARS-CoV-1 discovered that the phenotype of N-mediated PB disassembly was not
396 conserved among N proteins but was unique to SARS-CoV-2-N, and perhaps SARS-CoV-1 N
397 protein which appeared to disassemble PBs in two of three independent experiments (Fig 8).
398 Despite conservation of structural motifs, the N proteins between most human CoVs possess low
399 sequence conservation at the amino acid level (~25-50%) and have been reported to exhibit
400 different properties [115] . In contrast, SARS-CoV and SARS-CoV-2 N proteins have ~94%
401 amino acid identity [116], making it difficult to reconcile our observation that PB disassembly
402 induced by SARS-CoV-2 N protein was significant, while PB disassembly induced by SARS-
403 CoV-1 N protein was not (Fig 8). One difference that we observed by immunoblotting was the
404 presence of a lower molecular weight ~37 kDa band recognized by our anti-N antibody for
405 SARS-CoV-2. We did not observe the 37kDa N product after OC43 infection, transduction with
406 OC43 N protein or transduction with C-terminally Flag-tagged N proteins from 229E, NL63,
407 MERS-CoV or SARS-CoV-1 (Fig 3, Fig 8). Steady state levels of the lower molecular weight N
408 product increased over the course of SARS-CoV-2 infection, consistent with the timing of PB
409 disassembly. Other groups have noted that the SARS-CoV-2 variant of concern (VOC), Alpha,

410 produces an additional subgenomic mRNA from which a truncated version of N, termed N*, can
411 be produced [68,117,118]. Translation of the N* ORF is predicted to start at an internal in-frame
412 methionine residue (Met210) within the N protein [117,118]. Alignment of the SARS-CoV-2 N
413 protein sequence against other N proteins revealed that of the human CoVs, only SARS-CoV-1
414 and SARS-CoV-2 N retained a methionine at position 210 (229E: NC_002645.1, HKU1:
415 NC_006577.2, MERS: NC_019843.3, NL63: NC_005831.2, OC43: NC_006213.1, SARS-1:
416 NC_004718.3, SARS-2: NC_045512.2). However, a lower molecular weight N protein product
417 was not observed on our immunoblots for SARS-CoV N protein, leading us to speculate that the
418 downstream Met residue may not be used for translation initiation in this case. Viruses capitalize
419 on downstream methionine residues to translate truncated protein products with subcellular
420 localization or functions that differ from their full-length counterparts as a clever way to increase
421 coding capacity [119,120] . Our ongoing investigation of the precise nature of the SARS-CoV-2
422 N protein truncation product we observe during infection and overexpression may reveal that it
423 has a specific role in PB disassembly.
424
425 The PB protein MOV10, and other components of RNA processing machinery, were revealed as
426 potential interactors with the N protein [121] ; however, we do not observe colocalization of N
427 protein with PBs after immunofluorescent staining of SARS-CoV-2 infected cells or N-
428 expressing cells. Based on our data, we consider two possible mechanisms of N protein mediated
429 PB disassembly. First, N protein may mediate PB disassembly by phase separation with a PB
430 protein(s). This is similar to what has already been shown for N-mediated disruption of
431 cytoplasmic stress granules, important cytoplasmic biomolecular condensates that correlate with
432 cellular translational shutdown [35]. N protein localizes to stress granules and binds the essential

433 protein, G3BP1, preventing its interaction with other stress granule proteins and blocking stress
434 granule formation [122-124]. Although the precise domain required for this effect has been
435 debated, more than one report suggests that the N-terminal intrinsically disordered region is
436 required for stress granule disruption [123,125] . Second, a possible reason for PB loss may be
437 the indiscriminate binding of RNA by N protein. N protein could be acting as sponge for RNA,
438 pulling it out of cytoplasm, thereby reducing the RNA-protein interactions required for phase
439 separation of PBs [24,122]. We are currently engaged in site-directed and truncation mutagenesis
440 studies to determine the precise region(s) of SARS-CoV-2- N that is essential for PB
441 disassembly.
442
443 Prior to this report, little was known about CoVs and PBs, and the information that was
444 published was contradictory. Infection with murine hepatitis virus (MHV) was reported to
445 increase PBs, whereas transmissible gastroenteritis coronavirus (TGEV) decreased PBs [86,87].
446 Since the initiation of our study, one additional publication used ectopic expression of one of the
447 SARS-CoV-2 CoV proteases, nsp5, to test if it was capable of PB disassembly. Consistent with
448 the results of our screen (Fig 6), nsp5 did not mediate PB loss [32]. In this manuscript, we now
449 confirm that SARS-CoV-2, OC43, and 229E induce PB disassembly (Fig 1-3) [34] . We also
450 observed that different human CoVs cause PB loss using different viral gene products; SARS-
451 CoV-2 utilizes N protein but OC43 and 229E do not, a diversity which further underscores that
452 convergence on PB disassembly by viruses likely benefits viral replication. Because PBs are
453 composed of numerous cellular molecules with established (e.g. APOBEC, MOV10) or potential
454 (decapping enzymes and exonucleases that could degrade viral RNA) antiviral activities, it is
455 possible that viruses may target PBs for disassembly to negate their antiviral activity

456 [28,29,31,39-45,126]. A recent screen for cellular proteins that bind SARS-CoV-2 viral RNA
457 captured two PB proteins (Lsm14a and MOV10), which suggests CoV RNA may be shuttled to
458 PBs [127]. That said, our evidence does not yet discern if the proposed antiviral role of PB-
459 localized enzymes is promoted by phase separation of molecules into PBs or not; if so, we would
460 predict that the antiviral function of these molecules is lost when PB granules decondense.
461 Emerging evidence suggests that activity of the decapping enzymatic complex is increased by
462 phase separation and decreased in solution [9,24,128]. Thus, we speculate that PBs are direct-
463 acting antiviral granules that can restrict virus infection when present as visible condensates; for
464 this reason, they are targeted for disassembly by most viruses.
465
466 One possibility is that PBs are antiviral because their proteins help the cell respond to signals that
467 activate innate immune pathways [28,30,129,130]. In support of this, TRAF6 was shown to
468 control Dcp1a localization to PBs using ubiquitylation, suggesting that antiviral signaling is
469 more complex than previously appreciated and integrates transcriptional responses with cytokine
470 mRNA suppression in PBs [129,131] . Moreover, the PB protein Lsm14A has been shown to
471 bind to viral RNA/DNA after infection-induced PB disassembly to promote IRF3 activation and
472 IFN-β production [130]. Although it remains unclear if the higher order condensation of many
473 proteins into PBs is required for their proposed antiviral activity, what is clear is that the
474 outcome of PB disassembly is a reversal of the constitutive decay or translational suppression of
475 cytokine mRNA that would normally occur there [7,12-15,132] . Our data support a role for PBs
476 as sensors of virus infection that release cytokine transcripts from repression when they
477 disassemble. Using IF-FISH, we observed that RNAs encoding IL-6 and TNF, two molecules
478 elevated in severe SARS-CoV-2 disease, localized to PBs. Upon SARS-CoV-2 N-induced PB

479 disassembly, these transcripts re-localized from PB foci to the cytoplasm, a redistribution that
480 was also accompanied by an increase in FISH probe signal intensity signifying increase RNA
481 abundance (Fig 9). Although we did not see a statistically significant increase in IL-6 and TNF
482 RNA level in SARS-CoV-2 N-expressing cells using a population-based assay like RT-qPCR
483 (Fig 10), our single-cell analysis by IF-FISH suggests that the biological relevance of our
484 observation derives from the combination of increased transcript level abundance and the
485 redistribution of cytokine transcripts from PB foci to the cytoplasm. We speculate that viral
486 infection causes PB loss and this event is viewed as a danger signal by the cell: it relieves
487 cytokine mRNA suppression and re-localizes these transcripts, returning them to the cytoplasmic
488 pool of RNA to permit translation of proinflammatory cytokines that then act as a call for
489 reinforcements. In this way, PB disassembly is connected to the innate immune response and is
490 one of many signals that notify the immune system that a cell is infected. In situations where
491 interferon responses are delayed or defective, as is emerging for SARS-CoV-2 and severe
492 COVID-19 [65-67], PB disassembly may occur to alert the immune system of an infection, and
493 may be a contributing factor to pathogenic cytokine responses.
494
495 In summary, our work adds to a growing body of literature which describes that many viruses
496 target PBs for disassembly, supporting the idea that PBs restrict viral infection. We showed that
497 the N protein of SARS-CoV-2 is sufficient for PB disassembly, and this phenotype correlated
498 with elevated levels of PB-localized cytokine transcripts encoding IL-6 and TNF, both which are
499 elevated during SARS-CoV2 infection [53]. Not only does this work describe a previously
500 uncharacterized cellular event that occurs during CoV infection, but we have identified a novel

501 mechanism which may contribute to the dysregulated cytokine response exhibited by severe

502 SARS-CoV-2 infection.

503

504

505

506 **Materials and Methods**

507 **Cell Culture and Drug Treatments**

508 All cells were maintained in humidified 37 °C incubators with 5% CO_2 and 20% O_2. Vero E6
509 (ATCC), HEK293T cells (ATCC), HeLa Tet-Off cells (Clontech) and HeLa Flp-In TREx GFP-
510 Dcp1a cells (a generous gift from Dr. Anne-Claude Gingras) were cultured in DMEM (Thermo
511 Fisher) supplemented with 100 U/mL penicillin, 100 µg/mL streptomycin, 2 mM L-glutamine
512 (Thermo Fisher) and 10% FBS (Thermo Fisher). Calu3 (ATCC) and MRC-5 cells (ATCC, a
513 generous gift from Dr. David Proud) were cultured in EMEM (ATCC) supplemented with 100
514 U/mL penicillin, 100 µg/mL streptomycin, 2 mM L-glutamine and 10% FBS (Thermo Fisher).
515 HUVECs (Lonza) were cultured in endothelial cell growth medium (EGM-2) (Lonza). HUVECs
516 were seeded onto tissue culture plates or glass coverslips coated with 0.1 % (w/v) porcine gelatin
517 (Sigma) in 1x PBS. For sodium arsenite treatment, HUVECs were treated with 0.25 mM sodium
518 arsenite (Sigma) or a vehicle control for 30 min.

519 **Plasmids and Cloning**

520 pLenti-IRES-Puro SARS-CoV-2 plasmids were a generous gift from the Krogan Lab [96].
521 pLJM1-OC43-N was cloned from pGBW-m4134906, a gift from Ginkgo Bioworks & Benjie
522 Chen (Addgene plasmid #151960; http://n2t.net/addgene:151960; RRID:Addgene_151960)
523 using BamHI and EcoRI restriction sites (NEB). pLJM1-NL63-N-FLAG was cloned from
524 pGBW-m4134910, a gift from Ginkgo Bioworks & Benjie Chen (Addgene plasmid #151939;
525 http://n2t.net/addgene:151939; RRID:Addgene_151939) using BamHI and EcoRI. pLJM1-229E-
526 N-FLAG was cloned from pGBW-m4134902, a gift from Ginkgo Bioworks & Benjie Chen
527 (Addgene plasmid #151912; http://n2t.net/addgene:151912; RRID:Addgene151912) using
528 BamHI and EcoRI. Codon-optimized pLJM1-MERS-CoV-N-FLAG was cloned from

529 SinoBiological (cat #VG40068-CF) using BamHI and EcoRI (Table 1). Codon-optimized
530 pLJM1-SARS-CoV-N-FLAG was cloned SinoBiological (cat# VG40588-NF) using BamHI and
531 EcoRI. The Kaposi's sarcoma-associated herpesvirus Kaposin B (KapB, KS lung isolate) clone
532 in pLJM1 was previously described [91].

533 **Transient Transfections**

534 Transient transfections were performed using Fugene (Promega) according to manufacturer's
535 guidelines. Briefly, HeLa Flp-In TREx GFP-Dcp1a cells were seeded in 12-well plates at
536 150,000 cells/well in antibiotic-free DMEM. Cells were transfected with 1 µg of DNA and 3 µL
537 of Fugene for 48 hours before processing.

538 **Production and use of Recombinant Lentiviruses**

539 All recombinant lentiviruses were generated using a second-generation system. HEK293T cells
540 were transfected with psPAX2, MD2-G, and the lentiviral transfer plasmid containing a gene of
541 interest using polyethylenimine (PEI, Polysciences). 6 hours after transfection, serum-free media
542 was replaced with DMEM containing serum but no antibiotics. Viral supernatants were
543 harvested 48 hours post-transfection and frozen at -80°C until use. For transduction, lentiviruses
544 were thawed at 37°C and added to target cells in complete media containing 5 µg/mL polybrene
545 (Sigma). After 24 hours, the media was replaced with selection media containing 1 µg/mL
546 puromycin or 5 µg/mL blasticidin (ThermoFisher) and cells were selected for 48 h before
547 proceeding with experiments.

548 **Immunofluorescence**

549 Cells were seeded onto 18mm round, #1.5 coverslips (Electron Microscopy Sciences) for
550 immunofluorescence experiments. Following treatment, cells were fixed for 10 or 30 (if infected
551 with SARS-CoV-2) min in 4% (v/v) paraformaldehyde (Electron Microscopy Sciences).

552 Samples were permeabilized with 0.1% (v/v) Triton X-100 (Sigma-Aldrich) for 10 min at room
553 temperature and blocked in 1% human AB serum (Sigma-Aldrich) in 1X PBS 1 h at room
554 temperature. Primary and secondary antibodies (Table 2) were diluted in 1% human AB serum
555 and used at the concentrations in Table 2. Nuclei were stained with 1 µg/ml Hoechst
556 (Invitrogen). Samples were mounted with Prolong Gold AntiFade mounting media
557 (ThermoFisher). Images were captured using a Zeiss AxioObserver Z1 microscope with the 40X
558 oil-emersion objective unless otherwise stated in the respective figure caption. To account for
559 variability in staining, all experiments contained internal controls (negative control; mock or
560 EV). During image acquisition, exposure time was kept consistent within an independent
561 experiment.

562 **Immunofluorescence (IF) RNA Fluorescent *In Situ* Hybridization (FISH)**

563 IF-FISH was performed according to manufacturers protocol (Stellaris IF-FISH protocol).
564 Briefly, cells were fixed in 4% formaldehyde (Sigma-Aldrich) for 10 mins then permeabilized
565 with 0.1% Triton X-100 (Sigma-Aldrich) in PBS for 10 mins. Primary Hedls antibody was
566 diluted in PBS and incubated for 1 h at room temp, following which secondary antibody was
567 likewise diluted in PBS and allowed to incubate for 1 h at room temp. Cells were again fixed in
568 4% formaldehyde for 10 mins, washed with 1X PBS, and incubated in Wash Buffer A (LGC
569 Biosearch) for 5 minutes. Stellaris probes; GAPDH Quasar 670 (VSMF 2151-5), IL-6 Quasar
570 670 (LGC Biosearch, SMF 1065-5, custom order, probe sequences detailed in Table 4) and TNF
571 Quasar-670 (LGC Biosearch, SMF 1065-5, custom order, probe sequences detailed in Table 4).
572 were diluted in Hybridization Buffer (LGC Biocearch) to a concentration of 125 nM and cells
573 were incubated for hybridization at 37 °C overnight. The following day, cells were washed
574 sequentially with Wash Buffer A for 30 mins, Wash Buffer A containing 5 ng/mL DAPI

575 (Invitrogen) for 30 mins, and Wash Buffer B (LGC Biosearch) for 5 minutes. Samples were
576 mounted with Prolong Gold AntiFade mounting media (ThermoFisher). Images were captured
577 on a Zeiss LSM 880 confocal microscope with the 63X oil-emersion objective. At least three z-
578 stacks were acquired per condition, maximal intensity projections (MIPs) are presented.

579 **Immunoblotting**

580 Cells were lysed in 2X Laemmli buffer and stored at -20°C until use. The DC Protein Assay
581 (Bio-Rad) was used to quantify protein concentration as per the manufacturer's instructions. 10-
582 15 µg of protein lysate was resolved by SDS-PAGE on TGX Stain-Free acrylamide gels
583 (BioRad). Total protein images were acquired from the PVDF membranes after transfer on the
584 ChemiDoc Touch Imaging system (BioRad). Membranes were blocked in 5% BSA in TBS-T
585 (Tris-buffered saline 0.1% Tween-20). Primary and secondary antibodies were diluted in 2.5%
586 BSA, dilutions can be found in Table 2. Membranes were visualized using Clarity Western ECL
587 substrate and the ChemiDoc Touch Imaging system (BioRad). Densitometry was conducted
588 using ImageJ, area under the curve for each band was calculated, normalized to the respective
589 actin loading control band, and presented as fold change.

590 **Quantitative PCR**

591 RNA was collected using the RNeasy Plus Mini Kit (Qiagen) according to the manufacturer's
592 instructions and stored at -80°C until further use. RNA concentration was determined using
593 NanoDrop One^{C} (ThermoFisher) and 500 ng of RNA was reverse transcribed using qScript XLT
594 cDNA SuperMix (QuantaBio) using a combination of random hexamer and oligo dT primers,
595 according to the manufacturer's instructions. Depending on starting concentration, cDNA was
596 diluted between 1:10 and 1:20 for qPCR experiments and SsoFast EvaGreen Mastermix (Biorad)
597 was used to amplify cDNA. The ΔΔquantitation cycle (Cq) method was used to determine the

598 fold change in expression of target transcripts using HPRT as a housekeeping control
599 gene. Variance in the mock or empty vector samples was calculated by dividing the ΔCt value of
600 a single replicate by the average ΔCt value of all replicates for that specific gene and condition.
601 qPCR primer sequences can be found in Table 3. (Table 3).

602 **Virus Stocks and Virus Propagation**

603 Experiments with SARS-CoV-2 and variants were conducted in a containment level-3 (CL3)
604 facility, and all standard operating procedures were approved by the CL3 Oversight Committee
605 and Biosafety Office at the University of Calgary. Stocks of SARS-CoV-2 Toronto-01 isolate
606 (SARS-CoV-2/SB3-TYAGNC) [90] , Alpha, Beta, Gamma and Delta were propagated in Vero
607 E6 cells. To produce viral stocks, Vero E6 cells were infected at an MOI of 0.01 for 1 hour in
608 serum-free DMEM at 37˚C. Following adsorption, DMEM supplemented with 2% heat
609 inactivated FBS and 100 U/mL penicillin/streptomycin/glutamine was added to the infected
610 wells. 24-60 hours post-infection (hpi), the supernatant was harvested and centrifuged at 500 x *g*
611 for 5 min to remove cellular debris. Virus stocks were aliquoted and stored at -80˚C for single
612 use. SARS-CoV-2 titres were enumerated using plaque assays on Vero E6 cells as previously
613 described [133] using equal parts 2.4% w/v semi-solid colloidal cellulose overlay (Sigma;
614 prepared in ddH_2O) and 2X DMEM (Wisent) with 1% heat inactivated FBS and 1% PSQ.
615 Experiments with hCoV-OC43 (ATCC VR-1558) and hCoV-229E (ATCC VR-740) were
616 conducted in under containment level-2 conditions. hCoV-OC43 and hCoV-229E were
617 propagated in Vero E6 and MRC-5 cells, respectively. Cells were infected at an MOI of 0.01 for
618 1 hour in serum-free media at 33˚C. Following adsorption, the viral inoculum was removed and
619 replaced with fresh media supplemented with 2% heat inactivated FBS and 100 U/mL
620 penicillin/streptomycin/glutamine. After 5-6 days post infection (dpi), the supernatant was

621 harvested and cellular debris was cleared by centrifugation. Virus stocks were aliquoted and
622 stored at -80˚C. hCoV-OC43 and hCoV-229E titres were enumerated using Reed and Muench
623 tissue-culture infectious dose 50% ($TCID_{50}$) in Vero E6 or MRC-5 cells, respectively.

624 **Virus Infection**

625 For experimental infections, cells were seeded into wells to achieve ~80% confluency at the time
626 of infection. The growth media was removed and replaced with 100 µL of viral inoculum diluted
627 in serum-free DMEM to reach the desired MOI and incubated at 37˚C for 1 hour, rocking the
628 plate every 10 min. Following incubation, the virus inoculum was removed and replaced with 1
629 mL of complete growth media.

630 **Processing Body and FISH Probe Intensity Quantification**

631 Processing bodies were quantified using an unbiased image analysis pipeline generated in the
632 freeware CellProfiler4.0.6 (cellprofiler.org) [134]. First, nuclear staining was used to identify
633 individual cells applying a binary threshold and executing primary object detection between 65
634 and 200 pixels for HUVECs/$HUVEC^{ACE2}$ and 40 and 200 pixels for Calu3s. For each identified
635 object (nuclei), the peripheral boundary of each cell was defined using the "Propagation"
636 function. Propagation distance was customized depending on cell type to account for variance in
637 cell size (150 pixel radius from the nuclei for HUVECs/$HUVEC^{ACE2}$, 60 pixel radius from nuclei
638 for Calu3s). Using a subtractive function to remove the nuclei from the total cell area, the
639 cytoplasm of each cell was defined. The cytoplasm area mask was then applied to the matched
640 image stained for PB proteins (DDX6 or Hedls) to count only cytoplasmic puncta. Importantly,
641 multiple nuclei in close proximity (e.g., within the propagation distance) would be divided into
642 mutually exclusive cells, such that a single PB could not be counted more than once. Cells were
643 stratified into 'positive cells' (staining for viral proteins or dsRNA) or 'bystander cells'. In

644 control treatments (e.g., mock infected or EV) PBs in all cells were quantified. In treatment cells
645 only 'positive cells' were quantified unless otherwise indicated in corresponding figure captions.
646 Background staining was reduced using the "Enhance Speckles" function. Only DDX6 or Hedls-
647 positive puncta with a defined size (3-13 pixels) and intensity range were quantified using
648 "global thresholding with robust background adjustments" function. All thresholds were
649 consistent within each replicate that used identical staining parameters. PBs were quantified per
650 cell, either control (EV or mock) or treatment (infected or viral protein expressing). For each
651 experiment, an equal number of control and treatment cells were analyzed. For Figure 5, puncta
652 counts were exported and RStudio was used for data analysis and PB numbers in treatment cells
653 were represented relative to control cells for ease of data interpretation, rather than raw PBs per
654 cell. For Figure 9, nuclei and cells were defined according to HUVEC boundaries as specified
655 above. Background of probe specific staining was reduced using a global thresholding strategy
656 with a minimum cross entropy method of execution. The MeasureImageIntensity function was
657 then used to identify the total intensity per image which was divided by the number of cells
658 identified within that image for a final readout of total intensity/cell. A minimum of 40 cells
659 were quantified per condition.

660 **Statistics**

661 All statistical analyses were performed using GraphPad Prism 9.0. 'Per cell' processing body
662 counts were plotted such that each independent biological replicate (including paired control and
663 treatment) could be visualized on a single graph. Given that per cell processing body counts are
664 naturally skewed and thus non-parametric, we elected to use rank-sum statistical methods
665 (Mann-Whitney U test and Kruskal Wallis test) when appropriate, as indicated in the
666 corresponding figure caption. In the case of Figure 7, a two-way ANOVA with a Tukey's post-

667 hoc analysis was used to determine significance to (1) avoid the false discovery rate associated
668 with multiple T-tests and (2) because sodium arsenite-induced processing bodies appeared to be
669 parametrically distributed. Parametric distribution was assumed on all normalized data (Fig 5, 6,
670 9, 10, S4, & S7) and therefore we elected to use unpaired T-tests or one-way ANOVAs with
671 Dunnett's post-hoc analysis, as indicated in the corresponding figure caption.
672
673
674

675 **Table 1: Plasmids**

Plasmid	Use	Source	Mammalian Selection
pLJM1-Puro	Empty Vector Control	[90] [129]	Puromycin
pLJM1-BSD	Empty Vector Control	[129]	Blasticidin
pLJM1-ACE2	Overexpression		Blasticidin
pMD2.G	Lentivirus Generation	Addgene #12259	N/A
psPAX2	Lentivirus Generation	Addgene #12260	N/A
pLJM1-OC43-N	Overexpression	Addgene #151960	Puromycin
pLJM1-229E-N-FLAG	Overexpression	Addgene #151912	Puromycin
pLJM1-NL63-N-FLAG	Overexpression	Addgene #151939	Puromycin
pLJM1-MERS-CoV-N-FLAG	Overexpression	SinoBiological #VG40068-CF	Puromycin
pLJM1-SARS-CoV-1-N-FLAG	Overexpression	SinoBiological # VG40588-NF	Puromycin
pLenti-SARS-CoV-2-IRES-strep	Overexpression library	N Krogan (UCSF) [114]	Puromycin

676

677

678

679

680

681

682

683

684

685

686

687

688 **Table 2: Antibodies**

Antibody	Species	Vendor/Catalog #	Application	Dilution
Strep-Tag II	Mouse	Sigma (71590-M)	Immunofluorescence Immunoblot	1:1000 1:1000
DDX6	Rabbit	Bethyl (A300-461)	Immunofluorescence Immunoblot	1:1000 1:1000
Hedls	Mouse	Santa Cruz (sc-8418)	Immunofluorescence Immunoblot	1:1000 1:1000
Dcp1a	Rabbit	Novus (H00055802-M06)	Immunoblot	1:1000
Xrn1	Mouse	Abcam (ab231197)	Immunoblot	1:1000
Coronavirus OC43 Nucleocapsid	Mouse	Millipore (MAB-9012)	Immunofluorescence Immunoblot	1:500 1:1000
SARS-CoV2 Nucleocapsid	Rabbit	Novus (NBP3-05730)	Immunofluorescence	1:1000
SARS-CoV2 Nucleocapsid	Mouse	Novus (NBP3-05706)	Immunofluorescence Immunoblot	1:1000 1:1000
dsRNA clone J2	Mouse	Millipore (MABE-1134)	Immunofluorescence	1:100
FLAG	Mouse	CST (8146)	Immunofluorescence Immunoblot	1:1000 1:1000
Actin HRP-conjugated	Rabbit	CST (5215)	Immunoblot	1:10,000

689
690
691
692
693
694
695
696
697
698
699
700
701
702
703

704 **Table 3: qPCR primers**

Target	Direction	Sequence 5'→3'
HPRT	Forward	CTTTCCTTGGTCAGGCAGTATAA
HPRT	Reverse	AGTCTGGCTTATATCCAACACTTC
18S	Forward	TTCGAACGTCTGCCCTATCAA
18S	Reverse	GATGTGGTAGCCGTTTCTCAGG
IL6	Forward	GAAGCTCTATCTCGCCTCCA
IL6	Reverse	TTTTCTGCCAGTGCCTCTTT
CXCL8	Forward	AAATCTGGCAACCCTAGTCTG
CXCL8	Reverse	GTGAGGTAAGATGGTGGCTAAT
IL-1β	Forward	CTCTCACCTCTCCTACTCACTT
IL-1β	Reverse	TCAGAATGTGGGAGCGAATG
TNF	Forward	TCGAACCCCGAGTGACAA
TNF	Reverse	AGCTGCCCCTCAGCTTG
GM-CSF	Forward	AAATGTTTGACCTCCAGGAGCC
GM-CSF	Reverse	ATCTGGGTTGCACAGGAAGTT
COX-2	Forward	CCCTTGGGTGTCAAAGGTAA
COX-2	Reverse	GCCCTCGCTTATGATCTGTC
229E 5' Leader	Forward	AGTTGCTTTTTAGACTTTGTGTCT
229E gRNA (ORF1a)	Reverse	CAAGTGTCACACGGTTGCAG
229E sgRNA (N)	Reverse	CCACGTTGTGGTTCAGATGC

705

706

707

708

709 **Table 4. Probes for RNA Fluorescent in situ hybridization**

Target:	IL-6	TNF
	gatagagcttctctttcgtt	cgtctgagggttgttttcag
	agaaggagttcatagctggg	gggtcagtatgtgagaggaa
	agaaggcaactggaccgaag	atcatgctttcagtgctcat
	cggctacatctttggaatct	caaagtgcagcaggcagaag
	aagaggtgagtggctgtctg	cggggttcgagaagatgatc
	atttgtttgtcaattcgttc	cttgagggtttgctacaaca
	agatgccgtcgaggatgtac	accagctggttatctctcag
	tcacacatgttactcttgtt	ctgatggtgtgggtgaggag
	tctttggaaggttcaggttg	tctggtaggagacggcgatg
	aagcatccatctttttcagc	ctcttgatggcagagaggag
	ctcctcattgaatccagatt	gatagatgggctcataccag
	tgatgattttcaccaggcaa	attgatctcagcgctgagtc
	ctggaggtactctaggtata	caaagtcgagatagtcgggc
	tcctcactactctcaaatct	aaagtagacctgcccagact
	tactcatctgcacagctctg	ctcctcacagggcaatgatc
	caggaactggatcaggactt	ttgggaaggttggatgttcg
	gggtggttattgcatctaga	gtctgaaggagggggtaata
	tgagatgagttgtcatgtcc	gtggtcttgttgcttaaagt
	aactccttaaagctgcgcag	ctgaatcccaggtttcgaag
	catgctacatttgccgaaga	ttgaattcttagtggttgcc
	acaggtttctgaccagaaga	agggatcaaagctgtaggcc
	aacataagttctgtgcccag	tggtctccagattccagatg
	ctcatacttttagttctcca	cattctggccagaaccaaag
	ttcaaactgcatagccactt	taggtgaggtcttctcaagt
	ccaagaaatgatctggctct	aaggtccacttgtgtcaatt
	atttgaggtaagcctacact	acatctggagagaggaaggc
		cgtgtctcaaggaagtctgg
		ctacatgggaacagcctatt
		caaaagaaggcacagaggcc
		ttggtcaccaaatcagcatt
		agaggctcagcaatgagtga
		gggcgattacagacacaact
		ctttatttctcgccactgaa

710
711
712
713

714 **Figure Legends**

715

716 **Figure 1. Processing bodies are absent in SARS-CoV-2 infected cells. A-D.** HUVECs were
717 transduced with recombinant lentiviruses expressing human ACE2 (HUVEC-ACE2), selected,
718 and infected with SARS-CoV-2 TO-1 isolate at an MOI of 3 or a time-matched mock infection
719 control. At 16 hpi or 24 hpi, cells were fixed and immunostained for SARS-CoV-2 N protein
720 (green) and DDX6 (A, white) or Hedls (C, white). Nuclei were stained with Hoechst (blue).
721 Representative images from one of three independent experiments are shown (A, C). PBs were
722 quantified using CellProfiler by measuring DDX6 puncta (B) and Hedls puncta (D) in SARS-
723 CoV-2-infected cells (thresholded by N protein staining) or in mock-infected cells. These data
724 represent three independent biological replicates ($n=3$) with >80 cells measured per condition
725 (mock and infected) per replicate. Each mock and infected replicate pair plotted independently
726 (B, D); mean (****, $p < 0.0001$). **E-H.** Calu3 cells were infected with SARS-CoV-2 TO-1isolate
727 (MOI =3) or time-matched mock-infected control. 24 hpi cells were fixed and immunostained for
728 SARS-CoV-2 N (green), DDX6 (E; white) or Hedls (G; white). Nuclei were stained with
729 Hoechst (blue). PBs were quantified using CellProfiler as in B and D (F, H). These data
730 represent three independent biological replicates ($n=3$) with >130 cells measured per condition
731 (mock and infected) per replicate. Representative images from one experiment of three are
732 shown (E, G) and each mock and infected replicate pair plotted independently (F, H); mean
733 (****, $p < 0.0001$). Statistics were performed using a Mann-Whitney rank-sum test. Scale bar =
734 20 μm.

735 **Figure 2. Processing bodies are absent in SARS-CoV-2 alpha, beta, gamma, and delta**
736 **variant infected cells. A.** HUVECs were transduced with recombinant lentiviruses expressing

737 human ACE2 (HUVEC-ACE2), selected and infected with SARS-CoV-2 TO-1, alpha, beta,
738 gamma, or delta isolates (MOI=2), or a mock infection control. 24 hpi cells were fixed and
739 immunostained for SARS-CoV-2 N protein (green) and Hedls (white). Nuclei were stained with
740 Hoechst (blue). Representative images from one of two independent experiments are shown. **B.**
741 PBs were quantified as in Figure 1. These data represent two independent biological replicates
742 (*n=2*) with >80 cells measured per condition (mock and infected) per replicate. Each mock and
743 infected replicate pair plotted independently; mean. Statistics were performed using Kruskal-
744 Wallis H test with Dunn's correction (*, $p < 0.0332$; ****, $p < 0.0001$). Scale bar = 20 μM.

745 **Figure 3. Processing bodies are absent in OC43 and 229E infected cells. A-B.** HUVECs were
746 infected with OC43 ($TCID_{50} = 2 \times 10^4$) or mock-infected. Cells were fixed at 12 hpi or 24 hpi
747 and immunostained for DDX6 (PBs; white) and OC43 N protein (green). Nuclei were stained
748 with Hoechst (blue). These data represent three independent biological replicates (*n=3*) with >80
749 cells measured per condition (mock and infected) per replicate. Representative images from one
750 of three experiments are shown. DDX6 puncta in mock or OC43-infected cells were quantified
751 as in Figure 1. Each mock and infected replicate pair plotted independently; mean. **C-D.**
752 HUVECs were infected with 229E ($TCID_{50} = 2.4 \times 10^3$) or mock-infected. Cells were fixed at 6
753 hpi or 12 hpi and immunostained for DDX6 (PBs; white) and double-stranded RNA (proxy for
754 229E infection; green). Nuclei were stained with Hoechst (blue). These data represent three
755 independent biological replicates (*n=3*) with >80 cells measured per condition (mock and
756 infected) per replicate. Representative images from one of three experiments are shown. DDX6
757 puncta in mock or 229E-infected (dsRNA+) cells were quantified as in Figure 1. Each mock and
758 infected replicate pair plotted independently; mean. Statistics were performed using a Mann-
759 Whitney rank-sum test (****, $p < 0.0001$). Scale bar = 20 μM.

760 **Figure 4. Coronavirus infection does not alter steady state levels of most processing body**
761 **proteins. A.** HUVECs were transduced with human ACE2, selected, and infected with SARS-
762 CoV-2 TO-1 isolate (MOI=3). Cells were lysed at 6 and 12 hpi and immunoblotting was
763 performed using XRN1, Hedls, DCP1A, DDX6, SARS-CoV-2 N, and β-actin specific
764 antibodies. One representative experiment of two is shown. **B-C.** HUVECs were infected with
765 OC43 (B, $TCID_{50} = 2 \times 10^4$) or 229E (C, $TCID_{50} = 2.4 \times 10^3$). Cells were lysed at 12 and 24 hpi
766 (B, OC43) or 6 and 12 hpi (C, 229E). Immunoblotting was performed using XRN1, Hedls,
767 DCP1A, DDX6, OC43 N protein (B only), and β-actin specific antibodies. One representative
768 experiment of three is shown.
769
770 **Figure 5. Steady state levels of selected ARE-mRNAs are elevated during coronavirus**
771 **infection. A.** HUVECs were transduced with recombinant lentiviruses expressing human ACE2,
772 selected, and infected with SARS-CoV-2 TO isolate (MOI=3). RNA was harvested 24 hpi and
773 RT-qPCR was performed using IL-6, CXCL8, COX-2, GM-CSF, IL-1β and HPRT (house-
774 keeping gene) specific primers. Values are represented as fold change relative to mock-infection.
775 n=3; mean ± SD (*, $p < 0.05$; **, $p < 0.01$; ns, nonsignificant). **B-C.** HUVECs were infected with
776 OC43 (B, $TCID_{50}/mL = 3.5 \times 10^4$) or 229E (C, $TCID_{50}/mL = 1 \times 10^{3.24}$). RNA was harvested 24
777 and 12 hpi for OC43 (B) and 229E (C), respectively, and RT-qPCR was performed as in (A).
778 Values are represented as fold change relative to mock-infection. $n \geq 3$; mean ± SD (*, $p < 0.05$;
779 **, $p < 0.01$; ns, nonsignificant).
780
781 **Figure 6. Identification of SARS-CoV-2 ORFs that mediate processing body loss. A.** HeLa
782 cells expressing GFP-Dcp1a were transfected with an empty vector (EV) or 2xStrep-tagged

783 SARS-CoV-2 ORFs for 48 hours then fixed and immunostained for Strep-Tag-II (viral ORF;
784 green) or DDX6 (PBs; white). Nuclei were stained with Hoechst (blue). Staining of select ORFs
785 from one of three independent experiments are shown in A. **B.** As a positive control for PB
786 disassembly, HeLa GFP-Dcp1a cells were transfected with EV or the Kaposi's sarcoma-
787 associated herpesvirus (KSHV) protein, KapB for 48 hours then fixed and immunostained for
788 KapB (green) or Hedls (PBs; white). Nuclei were stained with Hoechst (blue); Scale bar = 20
789 μm. **C.** Hedls puncta were quantified as in Figure 1. These data represent three independent
790 replicates (*n=3*). Statistics were performed using an unpaired T test; (**, $p < 0.01$). **D-E.** DDX6
791 puncta were quantified using CellProfiler. In D, SARS-CoV-2 ORF-expressing cells were
792 thresholded by Strep-Tag-II staining intensity. The intensity threshold used was defined as two
793 standard deviations above mean intensity in vector controls. Only DDX6 puncta in cells above
794 this threshold were counted. In E, Strep-Tag-II staining could not be visualized above this
795 threshold; therefore, DDX6 puncta in all cells were counted (unthresholded). Values are
796 expressed as a fold-change difference normalized to the vector control (hashed line). These data
797 represent three or more independent replicates ($n \geq 3$). A one-way ANOVA with a Dunnett's post-
798 hoc analysis was performed; bars represent SEM (**, $p < 0.01$). N=nucleocapsid protein,
799 E=envelope protein, M=membrane protein, S=spike protein **F.** HeLa GFP-Dcp1a cells were
800 transfected as in A. 48 hours post-transfection cells were lysed. Samples were resolved by SDS-
801 PAGE on 4-15% gradient gels and immunoblotted with a Strep-Tag II antibody.

802

803 **Figure 7. Ectopic expression of SARS-CoV-2 N elicits processing body disassembly. A-B.**
804 HUVECs were transduced with recombinant lentiviruses ectopically expressing 2xStrep-tagged
805 SARS-CoV-2 N or empty vector control (EV) and selected with puromycin for 48 hours.

806 Samples were fixed and immunostained for Strep-Tag-II (N; green) and DDX6 (PBs; white).
807 Nuclei were stained with Hoechst (blue). Representative images from one of three independent
808 experiments are shown (*n=3*). Scale bar = 20 µm. DDX6 puncta were quantified per field of
809 view using CellProfiler as in Figure 1. >30 cells were measured per condition (EV and N) per
810 replicate. Bars represent the mean. Mann-Whitney rank-sum test was performed (****, $p <$
811 0.0001). **C-F.** HUVECs were transduced and selected as in A, then treated with 0.25 mM sodium
812 arsenite ($NaAsO_2$) or a vehicle control (Untreated) for 30 min, fixed and immunostained for
813 either Hedls (C, white) or DDX6 (D, white) and SARS-CoV-2 N (green). Nuclei were stained
814 with Hoechst (blue). Scale bar = 20 µm. Representative images from one independent
815 experiment of three are shown. These data represent three (C, D) or four (E, F) independent
816 replicates, with >30 cells measured per condition per replicate. Hedls puncta (D) and DDX6
817 puncta (F) were quantified as in Figure 1. Bars represent the mean. Statistics were performed
818 using a two-way ANOVA with a Tukey's multiple comparisons test (*, $p < 0.0332$; ****, $p <$
819 0.0001; ns, nonsignificant).
820

821 **Figure 8. Processing body disassembly is not a common feature of all human coronavirus N**
822 **proteins. A-D.** HUVECs were transduced with recombinant lentiviruses ectopically expressing
823 N protein from the betacoronaviruses MERS-CoV and OC43 (A-B) or N protein from
824 alphacoronaviruses 229E and NL63 (C-D) or N protein from SARS-CoV-1 (E-F). A control
825 lentiviral expressing an empty vector (EV) was used as a negative control and SARS-CoV-2 N
826 protein expressing lentiviruses were used as a positive control in each experiment. Cells were
827 selected, fixed and immunostained for DDX6 (PBs; white) and either authentic N protein or a
828 FLAG tag (green). Nuclei were stained with Hoechst (blue). Scale bar = 20 µm. DDX6 puncta in

829 EV or N-transduced cells were quantified using CellProfiler as in Figure 1. DDX6 puncta were
830 quantified as in Figure 1. Representative images from one independent experiment of three are
831 shown. These data represent three independent biological replicates (*n=3*) with >30 cells
832 measured per condition (EV and N) per replicate. Each EV and N replicate pair plotted
833 independently; mean. Statistics were performed using Kruskal-Wallis H test with Dunn's
834 correction (*, $p < 0.0332$; **, $p < 0.0021$; ****, $p < 0.0001$; ns, nonsignificant). **G-I.** HUVECs
835 were transduced as above, protein lysate was harvested and immunoblotting was performed
836 using XRN1, Hedls, DCP1A, DDX6, N protein or FLAG, and β-actin specific antibodies. One
837 representative experiment of three is shown.

838 **Figure 9. ARE-mRNAs colocalize with processing bodies. A.** HUVECs were treated with 0.01
839 ng/L soluble TNF to increase transcription of ARE-containing cellular mRNAs for 24 hours.
840 Cells were fixed and immunostained for Hedls prior to hybridization with Stellaris probes
841 specific for GAPDH, IL-6 and TNF. Nuclei were stained with Dapi. Cells were imaged using a
842 Zeiss LSM 880 confocal microscope with Airyscan using the 63x objective. At least three Z-
843 stacks were acquired per condition (probe) per replicate and a maximal intensity projection
844 (MIP) image is presented. One representative experiment of three is shown. Scale bar = 5 µm. **B-**
845 **C.** HUVECs were transduced with recombinant lentiviruses ectopically expressing SARS-CoV-2
846 N or an EV control. Cells were selected, fixed and immunostained for Hedls prior to
847 hybridization with Stellaris probes specific for GAPDH, IL-6 and TNF. Nuclei were stained with
848 Dapi. Only probe-specific staining is displayed for simplicity. Scale bar = 20 µm. Representative
849 images from one of two independent experiments are shown. Total signal intensity per cell was
850 quantified using CellProfiler and is represented as fold-change relative to the intensity in the EV
851 control.

852

853 **Figure 10. Ectopic expression of SARS-CoV-2 N elevates selected ARE-mRNAs. A-C.**
854 HUVECs were transduced with recombinant lentiviruses ectopically expressing alpha- and
855 betacoronavirus N proteins or empty vector (EV) control, selected, and treated with 0.01 ng/L
856 soluble TNF to increase transcription of ARE-containing cellular mRNAs. Total RNA was
857 harvested at 0, 8, 12, and 24 hours post TNF treatment and RT-qPCR was performed using IL-6
858 (A), CXCL8 (B), TNF (C) and HPRT (house-keeping gene) specific primers. Values are
859 represented as fold-change relative to EV-transduced cells for each time point. These data
860 represent three independent experiments (*n=3*); mean ± SD.

861

862

863 **Supplemental Figure Legends**

864

865 **Figure S1. HUVEC-ACE2 cells are permissive to SARS-CoV-2. A.** HUVECs were
866 transduced with recombinant lentiviruses expressing human ACE2, selected, and infected with
867 SARS-CoV-2 (TO-1 isolate; MOI=3). 6- and 24-hours post-infection, virus-containing
868 supernatant was harvested and titrated by $TCID_{50}$ assay in VeroE6 cells. These data represent
869 two independent experiments (*n*=2); mean ± SD. **B-C.** HUVECs were transduced with ACE2 as
870 in A. Cells were fixed and immunostained for DDX6 (B) or Hedls (C) and quantified per field of
871 view using CellProfiler. These data represent two independent experiments (*n*=2) with >100 cells
872 measured per condition. Each EV and ACE2 replicate pair plotted independently; mean.
873 Statistics were performed using a Mann-Whitney rank-sum test (ns, nonsignificant).

874

875 **Figure S2. HUVECs are permissive to OC43 and 229E infection. A-B.** HUVECs were
876 infected with OC43 ($TCID_{50}$ = 2 x 10^4) or 229E ($TCID_{50}$ = 2.4 x 10^3). 6-, 12-, or 24 hpi, virus-
877 containing supernatant was harvested and titrated $TCID_{50}$ assay in VeroE6 (A) or MRC5 (B)
878 cells, respectively. These data represent two independent experiments (*n*=2); mean ± SD. **C.**
879 HUVECs were infected with 229E as in B or mock infected. Total RNA was harvested 12 hpi
880 and RT-qPCR was performed using primers specific to 229E genomic RNA (gRNA) or
881 subgenomic RNA8 (sgRNA8), or HPRT (cellular house-keeping gene). Cycle-threshold (Ct)
882 values for each primer pair were plotted. These data represent three independent experiments
883 (*n*=3); mean ± SD. Ct values greater than 35 were not deemed biologically relevant and therefore
884 are scored as N/A. **D.** PCR products from C. were resolved using agarose gel electrophoresis.
885 gRNA fragment migrated at the expected size of 285 bp. sgRNA fragment migrated at its
886 expected ~80 bp. Representative images from one of two independent experiments are shown.
887
888 **Figure S3. Hedls puncta are absent in OC43 and 229E infected cells. A.** HUVECs were
889 infected with OC43 ($TCID_{50}$ = 2 x 10^4) or mock-infected. 12 or 24 hpi cells were fixed and
890 immunostained for DDX6 (green) and Hedls (white). Nuclei were stained with Hoechst (blue).
891 Representative images from one of three independent experiments shown. **B.** Hedls puncta in
892 OC43-infected or mock-infected cells were quantified per field of view using CellProfiler. **C.**
893 HUVECs were infected with 229E ($TCID_{50}$ = 2.4 x 10^3) or mock-infected. 6 or 12 hpi cells were
894 fixed and immunostained for DDX6 (green) and Hedls (white). Nuclei were stained with
895 Hoechst (blue). Representative images from one of three independent experiments shown. **D.**
896 Hedls puncta in 229E-infected or mock-infected cells were quantified as in B. These data
897 represent three independent experiments (*n*=3) with ≥100 cells measured per condition per

898 replicate. Each mock and infected replicate pair plotted independently; mean. Statistics were
899 performed using a Mann-Whitney rank-sum test (****, $p < 0.0001$). Scale bar = 20 μm.
900
901 **Figure S4. Processing body protein densitometry after human coronavirus infection. A.**
902 HUVECs were transduced with human ACE2, selected, and infected with SARS-CoV-2 TO-1
903 isolate (MOI=3). Cells were lysed at 6 and 12 hpi and immunoblotting was performed using
904 XRN1, Hedls, DCP1A, DDX6, SARS-CoV-2 N, and β-actin specific antibodies. The results of
905 second independent experiment of two is shown. **B-C.** HUVECs were infected with OC43
906 ($TCID_{50} = 2 \times 10^4$) or 229E ($TCID_{50} = 2.4 \times 10^3$) or mock-infected. Cells were lysed at 12 and 24
907 hpi (B, OC43) or 6 and 12 hpi (C, 229E). Immunoblotting was performed using DDX6, Hedls,
908 XRN1, DCP1A, and actin. Protein densitometry was determined in ImageJ normalized to actin
909 and expressed as a fold-change relative to the 12 hpi (B; OC43) or 6 hpi (C; 229E) mock-
910 infected control. These data represent three independent biological replicates (n=3). A one-way
911 ANOVA with a Dunnett's post-hoc analysis was performed; mean; bars represent SD (*, $p <$
912 0.05).
913
914 **Figure S5. Ectopic expression of SARS-CoV-2 ORFs.** HeLa cells expressing GFP-Dcp1a were
915 transfected with an empty vector (EV) control or 2xStrep-tagged SARS-CoV-2 ORFs for 48
916 hours then fixed and immunostained for Strep-Tag-II (viral ORF; green) or DDX6 (PBs; white).
917 Nuclei were stained with Hoechst (blue). **A.** SARS-CoV-2 ORFs that could be detected by Strep-
918 Tag-II staining (thresholded ORFs). **B.** SARS-CoV-2 ORFs that could not be detected by Strep-
919 Tag-II staining (unthresholded ORFs). Representative images from one of three or more

920 independent experiments shown. Scale is the same for all images. N=nucleocapsid protein,
921 E=envelope protein, M=membrane protein, S=spike protein
922
923 **Figure S6. Validation of processing body loss induced by selected SARS-CoV-2 ORFs in**
924 **HUVECs. A.** HUVECs were transduced with recombinant lentiviruses expressing 2xStrep-
925 tagged SARS-CoV-2 nsp1, nsp14, ORF3b, and ORF7b constructs or control lentiviruses (EV)
926 and selected with puromycin for 48 hours. Cells were fixed and immunostained for Strep-Tag-II
927 (ORFs; green) and DDX6 (PBs; white). Nuclei were stained with Hoechst (blue). Representative
928 images from one of three independent experiments shown. Scale bar = 20 µm. **B.** DDX6 puncta
929 were quantified per field of view using CellProfiler. These data represent three independent
930 experiments (n=3) with >18 cells measured per condition per replicate. Each EV and ORF-
931 expressing replicate pair plotted independently; mean. Statistics were performed using Kruskal-
932 Wallis H test with Dunn's correction (**, $p < 0.0021$; ****, $p < 0.0001$; ns, nonsignificant). **C.**
933 HUVECs were transduced as in A. Cells were lysed and immunoblotting was performed using
934 the Strep-Tag II antibody on a 4-15% gradient gel.
935
936 **Figure S7. Processing body protein densitometry after CoV N protein overexpression. A-C.**
937
938 HUVECs were transduced with recombinant lentiviruses ectopically expressing N protein from
939 the betacoronaviruses MERS-CoV and OC43 (A), N protein from alphacoronaviruses 229E and
940 NL63 (B) or SARS-CoV-1 N (C). A control lentiviral expressing an empty vector (EV) was used
941 as a negative control and SARS-CoV-2 N protein expressing lentiviruses were used as a positive
942 control in each experiment. Cells were selected and lysed and immunoblotting was performed
943 using XRN1, Hedls, DCP1A, DDX6, N protein or FLAG, and β-actin specific antibodies.

944 Protein densitometry was determined in ImageJ normalized to actin and expressed as a fold-
945 change relative to the EV control. These data represent three independent biological replicates
946 (n=3). A one-way ANOVA with a Dunnett's post-hoc analysis was performed; mean; bars
947 represent SD (*, $p < 0.05$).
948
949 **Figure S8. TNF treatment does not alter processing body number**
950 HUVECs were treated with 0.01 ng/L soluble TNF for either 6 or 12 hours following which,
951 cells were fixed and immunostained for Hedls. Nuclei were stained with Hoechst. Hedls puncta
952 were quantified per field of view using CellProfiler. These data represent two independent
953 experiments (n=2) with >90 cells measured per condition per replicate. Each mock and infected
954 replicate pair plotted independently; mean.
955
956

957 **Acknowledgements**

958 We sincerely thank the members of the Corcoran lab, Dr. Craig McCormick and Dr. Eric Pringle
959 for helpful discussions about this work. We would like to thank Dr. Nevan Krogan (UCSF) for
960 the SARS-CoV-2 gene library, Dr. David Proud (University of Calgary) for MRC-5 cells, and
961 Dr. Lorne Tyrrell, Dr. Michael Joyce and Holly Bandi (University of Alberta) for isolates of
962 SARS-CoV-2 variants Alpha, Beta, Gamma and Delta. We would like to thank Dr. Anne
963 Vaahtokari of the Charbonneau Microscopy Facility for microscopy support and Dr. Devender
964 Kumar for CL3 facility support. MK was supported by a CSM graduate training award, a CIHR
965 CGS-M scholarship, and a CIHR doctoral award and RPM was supported by a Snyder Institute
966 Beverley Phillips Doctoral training award. This study was supported by operating funds awarded
967 to JAC from the Canadian Institutes for Health Research (CIHR): a COVID rapid response
968 operating grant (#177704) and an operating grant (#175622) the Coronavirus Variants Rapid
969 Response Network (CoVaRR-Net), of which JAC is a member. The Vaccine and Infectious
970 Disease Organization (VIDO) receives operational funding for its CL3 facility (InterVac) from
971 the Canada Foundation for Innovation through the Major Science Initiatives. VIDO also receives
972 operational funding from the Government of Saskatchewan through Innovation Saskatchewan
973 and the Ministry of Agriculture.

974

975 **Author Contributions**

976 Mariel Kleer: Conceptualization, Experimentation, Analysis, Paper Writing

977 Rory P. Mulloy: Conceptualization, Experimentation, Analysis, Paper Writing

978 Carolyn-Ann Robinson: Conceptualization, Experimentation, Analysis, Paper Writing

979 Danyel Evseev: Experimentation, Analysis, Paper Writing

Maxwell P. Bui-Marinos: Experimentation, Analysis, Paper Writing

Elizabeth L. Castle: Analysis

Arinjay Banerjee: Reagents, Paper Editing

Samira Mubareka: Reagents

Karen Mossman: Reagents

Jennifer A. Corcoran: Conceptualization, Experimentation, Supervision, Funding Acquisition, Project Administration, Paper Writing

Conflict of Interest

The authors have no competing interests to declare.

991 **References**

992

993 1. Eulalio A, Behm-Ansmant I, Schweizer D, Izaurralde E. P-body formation is a
994 consequence, not the cause, of RNA-mediated gene silencing. Mol Cell Biol. 2007;27:
995 3970–3981. doi:10.1128/MCB.00128-07

996 2. Eulalio A, Rehwinkel J, Stricker M, Huntzinger E, Yang S-F, Doerks T, et al. Target-
997 specific requirements for enhancers of decapping in miRNA-mediated gene silencing.
998 Genes Dev. Cold Spring Harbor Lab; 2007;21: 2558–2570. doi:10.1101/gad.443107

999 3. Hubstenberger A, Courel M, Bénard M, Souquere S, Ernoult-Lange M, Chouaib R, et al.
1000 P-Body Purification Reveals the Condensation of Repressed mRNA Regulons. Mol Cell.
1001 Elsevier Inc; 2017;68: 144–157.e5. doi:10.1016/j.molcel.2017.09.003

1002 4. Youn J-Y, Dunham WH, Hong SJ, Knight JDR, Bashkurov M, Chen GI, et al. High-
1003 Density Proximity Mapping Reveals the Subcellular Organization of mRNA-Associated
1004 Granules and Bodies. Mol Cell. Elsevier Inc; 2018;69: 517–532.e11.
1005 doi:10.1016/j.molcel.2017.12.020

1006 5. Bakheet T, Hitti E, Khabar KSA. ARED-Plus: an updated and expanded database of
1007 AU-rich element-containing mRNAs and pre-mRNAs. Nucleic Acids Research.
1008 2018;46: D218–D220. doi:10.1093/nar/gkx975

1009 6. Hitti E, Bakheet T, Al-Souhibani N, Moghrabi W, Al-Yahya S, Al-Ghamdi M, et al.
1010 Systematic Analysis of AU-Rich Element Expression in Cancer Reveals Common
1011 Functional Clusters Regulated by Key RNA-Binding Proteins. Cancer Res. 2016;76:
1012 4068–4080. doi:10.1158/0008-5472.CAN-15-3110

1013 7. Blanco FF, Sanduja S, Deane NG, Blackshear PJ, Dixon DA. Transforming growth
1014 factor β regulates P-body formation through induction of the mRNA decay factor
1015 tristetraprolin. Mol Cell Biol. 2014;34: 180–195. doi:10.1128/MCB.01020-13

1016 8. Brengues M, Teixeira D, Parker R. Movement of eukaryotic mRNAs between
1017 polysomes and cytoplasmic processing bodies. Science. American Association for the
1018 Advancement of Science; 2005;310: 486–489. doi:10.1126/science.1115791

1019 9. Riggs CL, Kedersha N, Ivanov P, Anderson P. Mammalian stress granules and P bodies
1020 at a glance. J Cell Sci. 2020;133: jcs242487. doi:10.1242/jcs.242487

1021 10. Khong A, Parker R. mRNP architecture in translating and stress conditions reveals an
1022 ordered pathway of mRNP compaction. J Cell Biol. 2018;217: 4124–4140.
1023 doi:10.1083/jcb.201806183

1024 11. Matheny T, Rao BS, Parker R. Transcriptome-Wide Comparison of Stress Granules and
1025 P-Bodies Reveals that Translation Plays a Major Role in RNA Partitioning. Mol Cell
1026 Biol. 2019;39: 612. doi:10.1128/MCB.00313-19

1027 12. Corcoran JA, Khaperskyy DA, Johnston BP, King CA, Cyr DP, Olsthoorn AV, et al.
1028 Kaposi's sarcoma-associated herpesvirus G-protein-coupled receptor prevents AU-rich-
1029 element-mediated mRNA decay. J Virol. 2012;86: 8859–8871. doi:10.1128/JVI.00597-
1030 12

1031 13. Corcoran JA, Johnston BP, McCormick C. Viral Activation of MK2-hsp27-
1032 p115RhoGEF-RhoA Signaling Axis Causes Cytoskeletal Rearrangements, P-body
1033 Disruption and ARE-mRNA Stabilization. Robertson ES, editor. PLoS Pathogens.
1034 Public Library of Science; 2015;11: e1004597. doi:10.1371/journal.ppat.1004597

1035 14. Franks TM, Lykke-Andersen J. TTP and BRF proteins nucleate processing body
1036 formation to silence mRNAs with AU-rich elements. Genes Dev. 2007;21: 719–735.
1037 doi:10.1101/gad.1494707

1038 15. Vindry C, Marnef A, Broomhead H, Twyffels L, Ozgur S, Stoecklin G, et al. Dual RNA
1039 Processing Roles of Pat1b via Cytoplasmic Lsm1-7 and Nuclear Lsm2-8 Complexes.
1040 CellReports. 2017;20: 1187–1200. doi:10.1016/j.celrep.2017.06.091

1041 16. Vandelli A, Cid Samper F, Torrent Burgas M, Sanchez de Groot N, Tartaglia GG. The
1042 Interplay Between Disordered Regions in RNAs and Proteins Modulates Interactions
1043 Within Stress Granules and Processing Bodies. J Mol Biol. 2021;: 167159.
1044 doi:10.1016/j.jmb.2021.167159

1045 17. Nosella ML, Forman-Kay JD. Phosphorylation-dependent regulation of messenger RNA
1046 transcription, processing and translation within biomolecular condensates. Curr Opin
1047 Cell Biol. 2021;69: 30–40. doi:10.1016/j.ceb.2020.12.007

1048 18. Jalihal AP, Pitchiaya S, Xiao L, Bawa P, Jiang X, Bedi K, et al. Multivalent Proteins
1049 Rapidly and Reversibly Phase-Separate upon Osmotic Cell Volume Change. Mol Cell.
1050 2020;79: 978–990.e5. doi:10.1016/j.molcel.2020.08.004

1051 19. Mitrea DM, Chandra B, Ferrolino MC, Gibbs EB, Tolbert M, White MR, et al. Methods
1052 for Physical Characterization of Phase-Separated Bodies and Membrane-less Organelles.
1053 J Mol Biol. 2018;430: 4773–4805. doi:10.1016/j.jmb.2018.07.006

1054 20. Banani SF, Rice AM, Peeples WB, Lin Y, Jain S, Parker R, et al. Compositional Control
1055 of Phase-Separated Cellular Bodies. Cell. 2016;166: 651–663.
1056 doi:10.1016/j.cell.2016.06.010

1057 21. Guillén-Boixet J, Kopach A, Holehouse AS, Wittmann S, Jahnel M, Schlüßler R, et al.
1058 RNA-Induced Conformational Switching and Clustering of G3BP Drive Stress Granule
1059 Assembly by Condensation. Cell. 2020;181: 346–361.e17.
1060 doi:10.1016/j.cell.2020.03.049

1061 22. Van Treeck B, Parker R. Emerging Roles for Intermolecular RNA-RNA Interactions in
1062 RNP Assemblies. Cell. 2018;174: 791–802. doi:10.1016/j.cell.2018.07.023

1063 23. Cougot N, Cavalier A, Thomas D, Gillet R. The dual organization of P-bodies revealed
1064 by immunoelectron microscopy and electron tomography. J Mol Biol. 2012;420: 17–28.
1065 doi:10.1016/j.jmb.2012.03.027

1066 24. Corbet GA, Parker R. RNP Granule Formation: Lessons from P-Bodies and Stress
1067 Granules. Cold Spring Harb Symp Quant Biol. 2019;84: 203–215.
1068 doi:10.1101/sqb.2019.84.040329

1069 25. Standart N, Weil D. P-Bodies: Cytosolic Droplets for Coordinated mRNA Storage.
1070 Trends Genet. 2018;34: 612–626. doi:10.1016/j.tig.2018.05.005

1071 26. Docena G, Rovedatti L, Kruidenier L, Fanning A, Leakey NAB, Knowles CH, et al.
1072 Down-regulation of p38 mitogen-activated protein kinase activation and
1073 proinflammatory cytokine production by mitogen-activated protein kinase inhibitors in
1074 inflammatory bowel disease. Clin Exp Immunol. John Wiley & Sons, Ltd; 2010;162:
1075 108–115. doi:10.1111/j.1365-2249.2010.04203.x

1076 27. Jangra RK, Yi M, Lemon SM. DDX6 (Rck/p54) is required for efficient hepatitis C
1077 virus replication but not for internal ribosome entry site-directed translation. J Virol.
1078 2010;84: 6810–6824. doi:10.1128/JVI.00397-10

1079 28. Ng CS, Kasumba DM, Fujita T, Luo H. Spatio-temporal characterization of the antiviral
1080 activity of the XRN1-DCP1/2 aggregation against cytoplasmic RNA viruses to prevent
1081 cell death. Cell Death & Differentiation. Nature Publishing Group; 2020;36: 932–20.
1082 doi:10.1038/s41418-020-0509-0

1083 29. Ostareck DH, Naarmann-de Vries IS, Ostareck-Lederer A. DDX6 and its orthologs as
1084 modulators of cellular and viral RNA expression. Wiley Interdiscip Rev RNA. 2014;5:
1085 659–678. doi:10.1002/wrna.1237

1086 30. Dougherty JD, Tsai W-C, Lloyd RE. Multiple Poliovirus Proteins Repress Cytoplasmic
1087 RNA Granules. Viruses. Multidisciplinary Digital Publishing Institute; 2015;7: 6127–
1088 6140. doi:10.3390/v7122922

1089 31. Dougherty JD, White JP, Lloyd RE. Poliovirus-mediated disruption of cytoplasmic
1090 processing bodies. J Virol. 2011;85: 64–75. doi:10.1128/JVI.01657-10

1091 32. Fan S, Xu Z, Liu P, Qin Y, Chen M. Enterovirus 71 2A Protease Inhibits P-Body
1092 Formation To Promote Viral RNA Synthesis. J Virol. 2021;95: e0092221.
1093 doi:10.1128/JVI.00922-21

1094 33. Kanakamani S, Suresh PS, Venkatesh T. Regulation of processing bodies: From viruses
1095 to cancer epigenetic machinery. Cell Biol Int. John Wiley & Sons, Ltd; 2021;45: 708–
1096 719. doi:10.1002/cbin.11527

1097 34. Gaete-Argel A, Márquez CL, Barriga GP, Soto-Rifo R, Valiente-Echeverría F.
1098 Strategies for Success. Viral Infections and Membraneless Organelles. Front Cell Infect
1099 Microbiol. 2019;9: 336. doi:10.3389/fcimb.2019.00336

1100 35. McCormick C, Khaperskyy DA. Translation inhibition and stress granules in the
1101 antiviral immune response. Nature Reviews Immunology. Nature Publishing Group;
1102 2017;17: 647–660. doi:10.1038/nri.2017.63

1103 36. Tsai W-C, Lloyd RE. Cytoplasmic RNA Granules and Viral Infection. Annu Rev Virol.
1104 Annual Reviews; 2014;1: 147–170. doi:10.1146/annurev-virology-031413-085505

1105 37. Onomoto K, Jogi M, Yoo J-S, Narita R, Morimoto S, Takemura A, et al. Critical role of
1106 an antiviral stress granule containing RIG-I and PKR in viral detection and innate
1107 immunity. Kanai A, editor. PLoS ONE. Public Library of Science; 2012;7: e43031.
1108 doi:10.1371/journal.pone.0043031

1109 38. Abernathy E, Gilbertson S, Alla R, Glaunsinger B. Viral Nucleases Induce an mRNA
1110 Degradation-Transcription Feedback Loop in Mammalian Cells. Cell Host and Microbe.
1111 2015;18: 243–253. doi:10.1016/j.chom.2015.06.019

1112 39. Núñez RD, Budt M, Saenger S, Paki K, Arnold U, Sadewasser A, et al. The RNA
1113 Helicase DDX6 Associates with RIG-I to Augment Induction of Antiviral Signaling. Int
1114 J Mol Sci. Multidisciplinary Digital Publishing Institute; 2018;19: 1877.
1115 doi:10.3390/ijms19071877

1116 40. Balinsky CA, Schmeisser H, Wells AI, Ganesan S, Jin T, Singh K, et al. IRAV
1117 (FLJ11286), an Interferon-Stimulated Gene with Antiviral Activity against Dengue
1118 Virus, Interacts with MOV10. Diamond MS, editor. J Virol. 2017;91: 504.
1119 doi:10.1128/JVI.01606-16

1120 41. Wang H, Chang L, Wang X, Su A, Feng C, Fu Y, et al. MOV10 interacts with
1121 Enterovirus 71 genomic 5'UTR and modulates viral replication. Biochem Biophys Res
1122 Commun. 2016;479: 571–577. doi:10.1016/j.bbrc.2016.09.112

1123 42. Cuevas RA, Ghosh A, Wallerath C, Hornung V, Coyne CB, Sarkar SN. MOV10
1124 Provides Antiviral Activity against RNA Viruses by Enhancing RIG-I-MAVS-
1125 Independent IFN Induction. J Immunol. 2016;196: 3877–3886.
1126 doi:10.4049/jimmunol.1501359

1127 43. Burdick R, Smith JL, Chaipan C, Friew Y, Chen J, Venkatachari NJ, et al. P body-
1128 associated protein Mov10 inhibits HIV-1 replication at multiple stages. J Virol. 2010;84:
1129 10241–10253. doi:10.1128/JVI.00585-10

1130 44. Burgess HM, Mohr I. Cellular 5“-3” mRNA exonuclease Xrn1 controls double-stranded
1131 RNA accumulation and anti-viral responses. Cell Host and Microbe. 2015;17: 332–344.
1132 doi:10.1016/j.chom.2015.02.003

1133 45. Lumb JH, Li Q, Popov LM, Ding S, Keith MT, Merrill BD, et al. DDX6 Represses
1134 Aberrant Activation of Interferon- Stimulated Genes. CellReports. ElsevierCompany;
1135 2017;20: 819–831. doi:10.1016/j.celrep.2017.06.085

1136 46. V'kovski P, Kratzel A, Steiner S, Stalder H, Thiel V. Coronavirus biology and
1137 replication: implications for SARS-CoV-2. Nat Rev Microbiol. Nature Publishing
1138 Group; 2020;5: 536–16. doi:10.1038/s41579-020-00468-6

1139 47. Cui J, Li F, Shi Z-L. Origin and evolution of pathogenic coronaviruses. Springer US;
1140 2019;: 1–12. doi:10.1038/s41579-018-0118-9

1141 48. Banerjee A, Doxey AC, Tremblay BJ-M, Mansfield MJ, Subudhi S, Hirota JA, et al.
1142 Predicting the recombination potential of severe acute respiratory syndrome coronavirus
1143 2 and Middle East respiratory syndrome coronavirus. J Gen Virol. Microbiology
1144 Society; 2020;101: 1251–1260. doi:10.1099/jgv.0.001491

1145 49. Banerjee A, Doxey AC, Mossman K, Irving AT. Unraveling the Zoonotic Origin and
1146 Transmission of SARS-CoV-2. Trends Ecol Evol. 2021;36: 180–184.
1147 doi:10.1016/j.tree.2020.12.002

1148 50. Zhou H, Ji J, Chen X, Bi Y, Li J, Wang Q, et al. Identification of novel bat
1149 coronaviruses sheds light on the evolutionary origins of SARS-CoV-2 and related
1150 viruses. Cell. 2021;184: 4380–4391.e14. doi:10.1016/j.cell.2021.06.008

1151 51. Li W, Shi Z, Yu M, Ren W, Smith C, Epstein JH, et al. Bats are natural reservoirs of
1152 SARS-like coronaviruses. Science. American Association for the Advancement of
1153 Science; 2005;310: 676–679. doi:10.1126/science.1118391

1154 52. Fielding CA, Jones GW, McLoughlin RM, McLeod L, Hammond VJ, Uceda J, et al.
1155 Interleukin-6 signaling drives fibrosis in unresolved inflammation. Immunity. 2014;40:
1156 40–50. doi:10.1016/j.immuni.2013.10.022

1157 53. Blanco-Melo D, tenover BR. Imbalanced host response to SARS-CoV-2 drives
1158 development of COVID-19. Cell. 2020;: 1–46. doi:10.1016/j.cell.2020.04.026

1159 54. Pedersen SF, Ho Y-C. SARS-CoV-2: a storm is raging. Journal of Clinical Investigation.
1160 2020;130: 2202–2205. doi:10.1172/JCI137647

1161 55. Zou L, Ruan F, Huang M, Liang L, Huang H, Hong Z, et al. SARS-CoV-2 Viral Load in
1162 Upper Respiratory Specimens of Infected Patients. N Engl J Med. Massachusetts
1163 Medical Society; 2020;382: 1177–1179. doi:10.1056/NEJMc2001737

1164 56. Libby P, Lüscher T. COVID-19 is, in the end, an endothelial disease. Eur Heart J. 3rd
1165 ed. 2020;41: 3038–3044. doi:10.1093/eurheartj/ehaa623

1166 57. Chen G, Wu D, Guo W, Cao Y, Huang D, Wang H, et al. Clinical and immunological
1167 features of severe and moderate coronavirus disease 2019. J Clin Invest. American
1168 Society for Clinical Investigation; 2020;130: 2620–2629. doi:10.1172/JCI137244

1169 58. Pons S, Fodil S, Azoulay E, Zafrani L. The vascular endothelium: the cornerstone of
1170 organ dysfunction in severe SARS-CoV-2 infection. Crit Care. BioMed Central;
1171 2020;24: 353–8. doi:10.1186/s13054-020-03062-7

1172 59. Lowenstein CJ, Solomon SD. Severe COVID-19 is a Microvascular Disease.
1173 Circulation. Lippincott Williams & Wilkins Hagerstown, MD; 2020;191: 148.
1174 doi:10.1161/CIRCULATIONAHA.120.050354

1175 60. Varga Z, Flammer AJ, Steiger P, Haberecker M, Andermatt R, Zinkernagel AS, et al.
1176 Endothelial cell infection and endotheliitis in COVID-19. The Lancet. Elsevier Ltd;
1177 2020;395: 1417–1418. doi:10.1016/S0140-6736(20)30937-5

1178 61. Amraei R, Rahimi N. COVID-19, Renin-Angiotensin System and Endothelial
1179 Dysfunction. Cells. Multidisciplinary Digital Publishing Institute; 2020;9: 1652.
1180 doi:10.3390/cells9071652

1181 62. Teuwen L-A, Geldhof V, Pasut A, Carmeliet P. COVID-19: the vasculature unleashed.
1182 Nature Reviews Immunology. Nature Publishing Group; 2020;20: 389–391.
1183 doi:10.1038/s41577-020-0343-0

1184 63. Gu SX, Tyagi T, Jain K, Gu VW, Lee SH, Hwa JM, et al. Thrombocytopathy and
1185 endotheliopathy: crucial contributors to COVID-19 thromboinflammation. Nat Rev
1186 Cardiol. Nature Publishing Group; 2021;18: 194–209. doi:10.1038/s41569-020-00469-1

1187 64. Suvorava T, Kaesemeyer W. Targeting the Vascular Endothelium in the Treatment of
1188 COVID-19. J Cardiovasc Pharmacol. 2021;77: 1–3.
1189 doi:10.1097/FJC.0000000000000932

1190 65. Bastard P, Rosen LB, Zhang Q, Michailidis E, Hoffmann H-H, Zhang Y, et al. Auto-
1191 antibodies against type I IFNs in patients with life-threatening COVID-19. Science.
1192 2020;129: eabd4585. doi:10.1126/science.abd4585

1193 66. Zhang Q, Bastard P, Liu Z, Le Pen J, Moncada-Velez M, Chen J, et al. Inborn errors of
1194 type I IFN immunity in patients with life-threatening COVID-19. Science. 2020;:
1195 eabd4570. doi:10.1126/science.abd4570

1196 67. Park A, Iwasaki A. Type I and Type III Interferons - Induction, Signaling, Evasion, and
1197 Application to Combat COVID-19. Cell Host and Microbe. 2020;27: 870–878.
1198 doi:10.1016/j.chom.2020.05.008

1199 68. Thorne LG, Bouhaddou M, Reuschl A-K, Zuliani-Alvarez L, Polacco B, Pelin A, et al.
1200 Evolution of enhanced innate immune evasion by the SARS-CoV-2 B.1.1.7 UK variant.
1201 PlosPath. Cold Spring Harbor Laboratory; 2021;: 2021.06.06.446826.
1202 doi:10.1101/2021.06.06.446826

1203 69. Sposito B, Broggi A, Pandolfi L, Crotta S, Clementi N, Ferrarese R, et al. The interferon
1204 landscape along the respiratory tract impacts the severity of COVID-19. Cell. 2021;184:
1205 4953–4968.e16. doi:10.1016/j.cell.2021.08.016

1206 70. Ziegler CGK, Miao VN, Owings AH, Navia AW, Tang Y, Bromley JD, et al. Impaired
1207 local intrinsic immunity to SARS-CoV-2 infection in severe COVID-19. Cell. 2021;184:
1208 4713–4733.e22. doi:10.1016/j.cell.2021.07.023

1209 71. Zhou Z, Ren L, Zhang L, Zhong J, Xiao Y, Jia Z, et al. Heightened Innate Immune
1210 Responses in the Respiratory Tract of COVID-19 Patients. Cell Host and Microbe.
1211 2020;27: 883–890.e2. doi:10.1016/j.chom.2020.04.017

1212 72. Hadjadj J, Yatim N, Barnabei L, Corneau A, Boussier J, Smith N, et al. Impaired type I
1213 interferon activity and inflammatory responses in severe COVID-19 patients. Science.
1214 2020;369: 718–724. doi:10.1126/science.abc6027

1215 73. Banerjee A, El-Sayes N, Budylowski P, Jacob RA, Richard D, Maan H, et al.
1216 Experimental and natural evidence of SARS-CoV-2-infection-induced activation of type
1217 I interferon responses. iScience. 2021;24: 102477. doi:10.1016/j.isci.2021.102477

1218 74. Yuen C-K, Lam J-Y, Wong W-M, Mak L-F, Wang X, Chu H, et al. SARS-CoV-2
1219 nsp13, nsp14, nsp15 and orf6 function as potent interferon antagonists. Emerging
1220 Microbes & Infections. Taylor & Francis; 2020;9: 1418–1428.
1221 doi:10.1080/22221751.2020.1780953

1222 75. Miorin L, Kehrer T, Sanchez-Aparicio MT, Zhang K, Cohen P, Patel RS, et al. SARS-
1223 CoV-2 Orf6 hijacks Nup98 to block STAT nuclear import and antagonize interferon
1224 signaling. Proc Natl Acad Sci USA. 2020;5: 202016650–11.
1225 doi:10.1073/pnas.2016650117

1226 76. Banerjee AK, Blanco MR, Bruce EA, Honson DD, Chen LM, Chow A, et al. SARS-
1227 CoV-2 disrupts splicing, translation, and protein trafficking to suppress host defenses.
1228 Cell. Elsevier Inc; 2020;: 1–66. doi:10.1016/j.cell.2020.10.004

1229 77. Konno Y, Kimura I, Uriu K, Fukushi M, Irie T, Koyanagi Y, et al. SARS-CoV-2 ORF3b
1230 Is a Potent Interferon Antagonist Whose Activity Is Increased by a Naturally Occurring
1231 Elongation Variant. CellReports. 2020;32: 108185. doi:10.1016/j.celrep.2020.108185

1232 78. Yin X, Riva L, Pu Y, Martin-Sancho L, Kanamune J, Yamamoto Y, et al. MDA5
1233 Governs the Innate Immune Response to SARS-CoV-2 in Lung Epithelial Cells.
1234 CellReports. 2021;34: 108628. doi:10.1016/j.celrep.2020.108628

1235 79. Lei X, Dong X, Ma R, Wang W, Xiao X, Tian Z, et al. Activation and evasion of type I
1236 interferon responses by SARS-CoV-2. Nature Communications. Nature Publishing
1237 Group; 2020;11: 3810–12. doi:10.1038/s41467-020-17665-9

1238 80. Beyer DK, Forero A. Mechanisms of Antiviral Immune Evasion of SARS-CoV-2. J Mol
1239 Biol. 2021;: 167265. doi:10.1016/j.jmb.2021.167265

1240 81. Xia H, Cao Z, Xie X, Zhang X, Chen JY-C, Wang H, et al. Evasion of Type I Interferon
1241 by SARS-CoV-2. CellReports. 2020;33: 108234. doi:10.1016/j.celrep.2020.108234

1242 82. Suryawanshi RK, Koganti R, Agelidis A, Patil CD, Shukla D. Dysregulation of Cell
1243 Signaling by SARS-CoV-2. Trends in Microbiology. 2021;29: 224–237.
1244 doi:10.1016/j.tim.2020.12.007

1245 83. Wickenhagen A, Sugrue E, Lytras S, Kuchi S, Noerenberg M, Turnbull ML, et al. A
1246 prenylated dsRNA sensor protects against severe COVID-19. Science. American
1247 Association for the Advancement of Science; 2021;: eabj3624.
1248 doi:10.1126/science.abj3624

1249 84. Hsu JC-C, Laurent-Rolle M, Pawlak JB, Wilen CB, Cresswell P. Translational shutdown
1250 and evasion of the innate immune response by SARS-CoV-2 NSP14 protein. Proc Natl
1251 Acad Sci USA. National Academy of Sciences; 2021;118.
1252 doi:10.1073/pnas.2101161118

1253 85. Zhao Y, Sui L, Wu P, Wang W, Wang Z, Yu Y, et al. A dual-role of SARS-CoV-2
1254 nucleocapsid protein in regulating innate immune response. Signal Transduct Target
1255 Ther. Nature Publishing Group; 2021;6: 331–14. doi:10.1038/s41392-021-00742-w

1256 86. Sola I, Galán C, Mateos-Gómez PA, Palacio L, Zuñiga S, Cruz JL, et al. The
1257 polypyrimidine tract-binding protein affects coronavirus RNA accumulation levels and
1258 relocalizes viral RNAs to novel cytoplasmic domains different from replication-
1259 transcription sites. J Virol. 3rd ed. 2011;85: 5136–5149. doi:10.1128/JVI.00195-11

1260 87. Raaben M, Groot Koerkamp MJA, Rottier PJM, de Haan CAM. Mouse hepatitis
1261 coronavirus replication induces host translational shutoff and mRNA decay, with
1262 concomitant formation of stress granules and processing bodies. Cellular Microbiology.
1263 2007;9: 2218–2229. doi:10.1111/j.1462-5822.2007.00951.x

1264 88. Ackermann M, Mentzer SJ, Kolb M, Jonigk D. Inflammation and Intussusceptive
1265 Angiogenesis in COVID-19: everything in and out of Flow. Eur Respir J. 2020;383:
1266 2003147. doi:10.1183/13993003.03147-2020

1267 89. Nascimento Conde J, Schutt WR, Gorbunova EE, Mackow ER. Recombinant ACE2
1268 Expression Is Required for SARS-CoV-2 To Infect Primary Human Endothelial Cells
1269 and Induce Inflammatory and Procoagulative Responses. Patton JT, editor. mBio.
1270 American Society for Microbiology; 2020;11. doi:10.1128/mBio.03185-20

1271 90. Banerjee A, Nasir JA, Budylowski P, Yip L, Aftanas P, Christie N, et al. Isolation,
1272 Sequence, Infectivity, and Replication Kinetics of Severe Acute Respiratory Syndrome
1273 Coronavirus 2. Emerging Infect Dis. 2020;26: 2054–2063. doi:10.3201/eid2609.201495

1274 91. Castle EL, Robinson C-A, Douglas P, Rinker KD, Corcoran JA. Viral manipulation of a
1275 mechanoresponsive signaling axis disassembles processing bodies. Mol Cell Biol. 2021;:
1276 MCB0039921. doi:10.1128/MCB.00399-21

1277 92. Singh J, Pandit P, McArthur AG, Banerjee A, Mossman K. Evolutionary trajectory of
1278 SARS-CoV-2 and emerging variants. Virology Journal. BioMed Central; 2021;18: 166–
1279 21. doi:10.1186/s12985-021-01633-w

1280 93. Harvey WT, Carabelli AM, Jackson B, Gupta RK, Thomson EC, Harrison EM, et al.
1281 SARS-CoV-2 variants, spike mutations and immune escape. Nat Rev Microbiol. Nature
1282 Publishing Group; 2021;19: 409–424. doi:10.1038/s41579-021-00573-0

1283 94. Sola I, Almazán F, Zuñiga S, Enjuanes L. Continuous and Discontinuous RNA
1284 Synthesis in Coronaviruses. Annu Rev Virol. Annual Reviews; 2015;2: 265–288.
1285 doi:10.1146/annurev-virology-100114-055218

1286 95. Ayache J, Bénard M, Ernoult-Lange M, Minshall N, Standart N, Kress M, et al. P-body
1287 assembly requires DDX6 repression complexes rather than decay or Ataxin2/2L
1288 complexes. Matera AG, editor. Mol Biol Cell. The American Society for Cell Biology;
1289 2015;26: 2579–2595. doi:10.1091/mbc.E15-03-0136

1290 96. Gordon DE, Jang GM, Bouhaddou M, Xu J, Obernier K, White KM, et al. A SARS-
1291 CoV-2 protein interaction map reveals targets for drug repurposing. Nature. Nature
1292 Publishing Group; 2020;583: 459–468. doi:10.1038/s41586-020-2286-9

1293 97. Kleer M, MacNeil G, Adam N, Pringle ES, Corcoran JA. A panel of KSHV mutants in
1294 the polycistronic kaposin locus for precise analysis of individual protein products. J
1295 Virol. American Society for Microbiology 1752 N St., N.W., Washington, DC; 2021;:
1296 JVI0156021. doi:10.1128/JVI.01560-21

1297 98. Robinson C-A, Singh GK, Kleer M, Castle EL, Boudreau BQ, Corcoran JA. Kaposi's
1298 sarcoma-associated herpesvirus (KSHV) utilizes the NDP52/CALCOCO2 selective
1299 autophagy receptor to disassemble processing bodies. PLoS Pathogens. 2022;: 1–61.
1300 doi:10.1101/2021.02.07.430164

1301 99. Min Y-Q, Mo Q, Wang J, Deng F, Wang H, Ning Y-J. SARS-CoV-2 nsp1:
1302 Bioinformatics, Potential Structural and Functional Features, and Implications for
1303 Drug/Vaccine Designs. Front Microbiol. Frontiers; 2020;11: 587317.
1304 doi:10.3389/fmicb.2020.587317

1305 100. Zeng W, Liu G, Ma H, Zhao D, Yang Y, Liu M, et al. Biochemical characterization of
1306 SARS-CoV-2 nucleocapsid protein. Biochem Biophys Res Commun. 2020;527: 618–
1307 623. doi:10.1016/j.bbrc.2020.04.136

1308 101. Kedersha N, Stoecklin G, Ayodele M, Yacono P, Lykke-Andersen J, Fritzler MJ, et al.
1309 Stress granules and processing bodies are dynamically linked sites of mRNP remodeling.
1310 J Cell Biol. 2005;169: 871–884. doi:10.1083/jcb.200502088

1311 102. Bai Z, Cao Y, Liu W, Li J. The SARS-CoV-2 Nucleocapsid Protein and Its Role in Viral
1312 Structure, Biological Functions, and a Potential Target for Drug or Vaccine Mitigation.
1313 Viruses. Multidisciplinary Digital Publishing Institute; 2021;13: 1115.
1314 doi:10.3390/v13061115

1315 103. Peng T-Y, Lee K-R, Tarn W-Y. Phosphorylation of the arginine/serine dipeptide-rich
1316 motif of the severe acute respiratory syndrome coronavirus nucleocapsid protein
1317 modulates its multimerization, translation inhibitory activity and cellular localization.
1318 FEBS J. John Wiley & Sons, Ltd; 2008;275: 4152–4163. doi:10.1111/j.1742-
1319 4658.2008.06564.x

1320 104. McBride R, van Zyl M, Fielding BC. The coronavirus nucleocapsid is a multifunctional
1321 protein. Viruses. Multidisciplinary Digital Publishing Institute; 2014;6: 2991–3018.
1322 doi:10.3390/v6082991

1323 105. Cong Y, Ulasli M, Schepers H, Mauthe M, V'kovski P, Kriegenburg F, et al.
1324 Nucleocapsid Protein Recruitment to Replication-Transcription Complexes Plays a
1325 Crucial Role in Coronaviral Life Cycle. Dutch RE, editor. J Virol. American Society for
1326 Microbiology Journals; 2020;94: 181. doi:10.1128/JVI.01925-19

1327 106. Lu S, Ye Q, Singh D, Villa E, Cleveland DW, Corbett KD. The SARS-CoV-2
1328 Nucleocapsid phosphoprotein forms mutually exclusive condensates with RNA and the
1329 membrane-associated M protein. PlosPath. 2020;18: 479.
1330 doi:10.1101/2020.07.30.228023

1331 107. Cascarina SM, Ross ED. A proposed role for the SARS-CoV-2 nucleocapsid protein in
1332 the formation and regulation of biomolecular condensates. FASEB j. 2020;34: 9832–
1333 9842. doi:10.1096/fj.202001351

1334 108. Chen H, Cui Y, Han X, Hu W, Sun M, Zhang Y, et al. Liquid-liquid phase separation by
1335 SARS-CoV-2 nucleocapsid protein and RNA. Cell Res. Nature Publishing Group;
1336 2020;30: 1143–1145. doi:10.1038/s41422-020-00408-2

1337 109. Savastano A, Ibáñez de Opakua A, Rankovic M, Zweckstetter M. Nucleocapsid protein
1338 of SARS-CoV-2 phase separates into RNA-rich polymerase-containing condensates.
1339 Nature Communications. Nature Publishing Group; 2020;11: 6041–10.
1340 doi:10.1038/s41467-020-19843-1

1341 110. Iserman C, Roden CA, Boerneke MA, Sealfon RSG, McLaughlin GA, Jungreis I, et al.
1342 Genomic RNA Elements Drive Phase Separation of the SARS-CoV-2 Nucleocapsid.
1343 Mol Cell. 2020;80: 1078–1091.e6. doi:10.1016/j.molcel.2020.11.041

1344 111. Carlson CR, Asfaha JB, Ghent CM, Howard CJ, Hartooni N, Safari M, et al.
1345 Phosphoregulation of Phase Separation by the SARS-CoV-2 N Protein Suggests a
1346 Biophysical Basis for its Dual Functions. Mol Cell. 2020;80: 1092–1103.e4.
1347 doi:10.1016/j.molcel.2020.11.025

1348 112. Cubuk J, Alston JJ, Incicco JJ, Singh S, Stuchell-Brereton MD, Ward MD, et al. The
1349 SARS-CoV-2 nucleocapsid protein is dynamic, disordered, and phase separates with
1350 RNA. Nature Communications. Nature Publishing Group; 2021;12: 1936–17.
1351 doi:10.1038/s41467-021-21953-3

1352 113. Sa Ribero M, Jouvenet N, Dreux M, Nisole S. Interplay between SARS-CoV-2 and the
1353 type I interferon response. PLoS Pathogens. Public Library of Science; 2020;16:
1354 e1008737. doi:10.1371/journal.ppat.1008737

1355 114. Gori Savellini G, Anichini G, Gandolfo C, Cusi MG. SARS-CoV-2 N Protein Targets
1356 TRIM25-Mediated RIG-I Activation to Suppress Innate Immunity. Viruses.
1357 Multidisciplinary Digital Publishing Institute; 2021;13: 1439. doi:10.3390/v13081439

1358 115. Oliveira SC, de Magalhães MTQ, Homan EJ. Immunoinformatic Analysis of SARS-
1359 CoV-2 Nucleocapsid Protein and Identification of COVID-19 Vaccine Targets. Front
1360 Immunol. Frontiers; 2020;11: 587615. doi:10.3389/fimmu.2020.587615

1361 116. Chan JF-W, Kok K-H, Zhu Z, Chu H, To KK-W, Yuan S, et al. Genomic
1362 characterization of the 2019 novel human-pathogenic coronavirus isolated from a patient
1363 with atypical pneumonia after visiting Wuhan. Emerging Microbes & Infections. 2020;9:
1364 221–236. doi:10.1080/22221751.2020.1719902

1365 117. Parker MD, Lindsey BB, Leary S, Gaudieri S, Chopra A, Wyles M, et al. Subgenomic
1366 RNA identification in SARS-CoV-2 genomic sequencing data. Genome Res. Cold
1367 Spring Harbor Lab; 2021;31: 645–658. doi:10.1101/gr.268110.120

1368 118. Leary S, Gaudieri S, Parker MD, Chopra A, James I, Pakala S, et al. Generation of a
1369 Novel SARS-CoV-2 Sub-genomic RNA Due to the R203K/G204R Variant in
1370 Nucleocapsid: Homologous Recombination has Potential to Change SARS-CoV-2 at
1371 Both Protein and RNA Level. Pathog Immun. 2021;6: 27–49. doi:10.20411/pai.v6i2.460

1372 119. Saffran HA, Pare JM, Corcoran JA, Weller SK, Smiley JR. Herpes simplex virus
1373 eliminates host mitochondrial DNA. EMBO Rep. 2007;8: 188–193.
1374 doi:10.1038/sj.embor.7400878

1375 120. Corcoran JA, Saffran HA, Duguay BA, Smiley JR. Herpes simplex virus UL12.5 targets
1376 mitochondria through a mitochondrial localization sequence proximal to the N terminus.
1377 J Virol. 2009;83: 2601–2610. doi:10.1128/JVI.02087-08

1378 121. Gordon DE, Hiatt J, Bouhaddou M, Rezelj VV, Ulferts S, Braberg H, et al. Comparative
1379 host-coronavirus protein interaction networks reveal pan-viral disease mechanisms.
1380 Science. 2020;11: eabe9403–38. doi:10.1126/science.abe9403

1381 122. Nabeel-Shah S, Lee H, Ahmed N, Burke GL, Farhangmehr S, Ashraf K, et al. SARS-
1382 CoV-2 nucleocapsid protein binds host mRNAs and attenuates stress granules to impair
1383 host stress response. iScience. 2022;25: 103562. doi:10.1016/j.isci.2021.103562

1384 123. Luo L, Li Z, Zhao T, Ju X, Ma P, Jin B, et al. SARS-CoV-2 nucleocapsid protein phase
1385 separates with G3BPs to disassemble stress granules and facilitate viral production. Sci
1386 Bull (Beijing). 2021;66: 1194–1204. doi:10.1016/j.scib.2021.01.013

1387 124. Zheng Z-Q, Wang S-Y, Xu Z-S, Fu Y-Z, Wang Y-Y. SARS-CoV-2 nucleocapsid
1388 protein impairs stress granule formation to promote viral replication. Cell Discov.
1389 Nature Publishing Group; 2021;7: 38–11. doi:10.1038/s41421-021-00275-0

1390 125. Wang J, Shi C, Xu Q, Yin H. SARS-CoV-2 nucleocapsid protein undergoes liquid-liquid
1391 phase separation into stress granules through its N-terminal intrinsically disordered
1392 region. Cell Discov. Nature Publishing Group; 2021;7: 5–5. doi:10.1038/s41421-020-
1393 00240-3

1394 126. Dougherty JD, Reineke LC, Lloyd RE. mRNA decapping enzyme 1a (Dcp1a)-induced
1395 translational arrest through protein kinase R (PKR) activation requires the N-terminal
1396 enabled vasodilator-stimulated protein homology 1 (EVH1) domain. J Biol Chem.
1397 2014;289: 3936–3949. doi:10.1074/jbc.M113.518191

1398 127. Schmidt N, Lareau CA, Keshishian H, Ganskih S, Schneider C, Hennig T, et al. The
1399 SARS-CoV-2 RNA-protein interactome in infected human cells. Nat Microbiol. Nature
1400 Publishing Group; 2021;6: 339–353. doi:10.1038/s41564-020-00846-z

1401 128. Tibble RW, Depaix A, Kowalska J, Jemielity J, Gross JD. Biomolecular condensates
1402 amplify mRNA decapping by coupling protein interactions with conformational changes
1403 in Dcp1/Dcp2. 2020;60th Anniversary: 600–36. doi:10.1101/2020.07.09.195057

1404 129. Tenekeci U, Poppe M, Beuerlein K, Buro C, Müller H, Weiser H, et al. K63-
1405 Ubiquitylation and TRAF6 Pathways Regulate Mammalian P-Body Formation and
1406 mRNA Decapping. Mol Cell. 2016;62: 943–957. doi:10.1016/j.molcel.2016.05.017

1407 130. Li Y, Chen R, Zhou Q, Xu Z, Li C, Wang S, et al. LSm14A is a processing body-
1408 associated sensor of viral nucleic acids that initiates cellular antiviral response in the
1409 early phase of viral infection. Proc Natl Acad Sci USA. 2012;109: 11770–11775.
1410 doi:10.1073/pnas.1203405109

1411 131. Rzeczkowski K, Beuerlein K, Müller H, Dittrich-Breiholz O, Schneider H, Kettner-
1412 Buhrow D, et al. c-Jun N-terminal kinase phosphorylates DCP1a to control formation of
1413 P bodies. J Cell Biol. 2011;194: 581–596. doi:10.1083/jcb.201006089

1414 132. Stoecklin G, Mayo T, Anderson P. ARE-mRNA degradation requires the 5“-3” decay
1415 pathway. EMBO Rep. 2006;7: 72–77. doi:10.1038/sj.embor.7400572

1416 133. Mendoza EJ, Manguiat K, Wood H, Drebot M. Two Detailed Plaque Assay Protocols
1417 for the Quantification of Infectious SARS-CoV-2. Curr Protoc Microbiol. John Wiley &
1418 Sons, Ltd; 2020;57: cpmc105. doi:10.1002/cpmc.105

1419 134. Kamentsky L, Jones TR, Fraser A, Bray M-A, Logan DJ, Madden KL, et al. Improved
1420 structure, function and compatibility for CellProfiler: modular high-throughput image
1421 analysis software. Bioinformatics. 2011;27: 1179–1180.
1422 doi:10.1093/bioinformatics/btr095

1423 135. Johnston BP, Pringle ES, McCormick C. KSHV activates unfolded protein response
1424 sensors but suppresses downstream transcriptional responses to support lytic replication.
1425 Swaminathan S, editor. PLoS Pathogens. 2019;15: e1008185.
1426 doi:10.1371/journal.ppat.1008185

1427

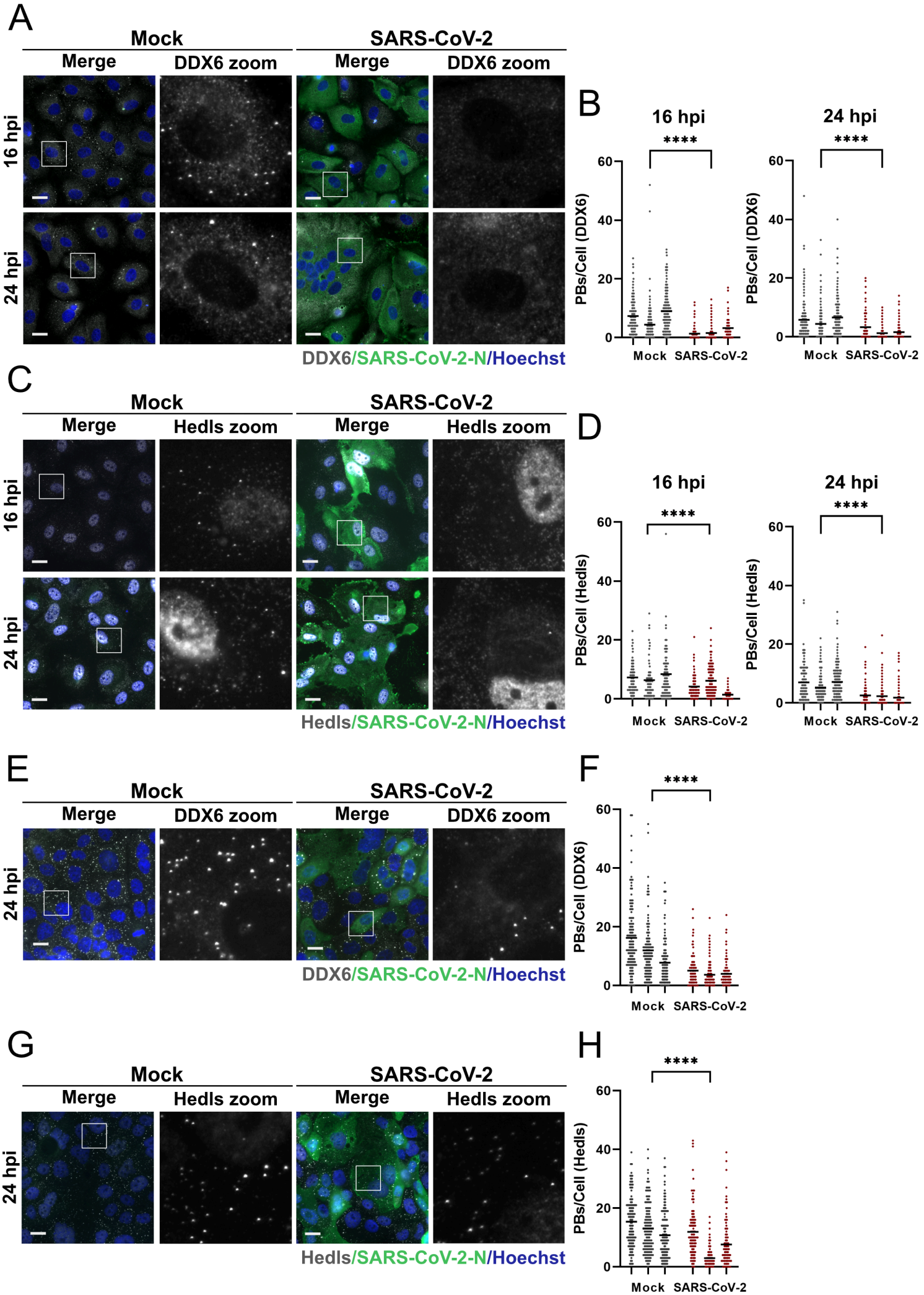
A
Mock
SARS-CoV-2
Merge
DDX6 zoom
16 hpi
24 hpi
DDX6/SARS-CoV-2-N/Hoechst
B
16 hpi
24 hpi
****
PBs/Cell (DDX6)
Mock
SARS-CoV-2
C
Hedls zoom
Hedls/SARS-CoV-2-N/Hoechst
D
PBs/Cell (Hedls)
E
F
G
H

A

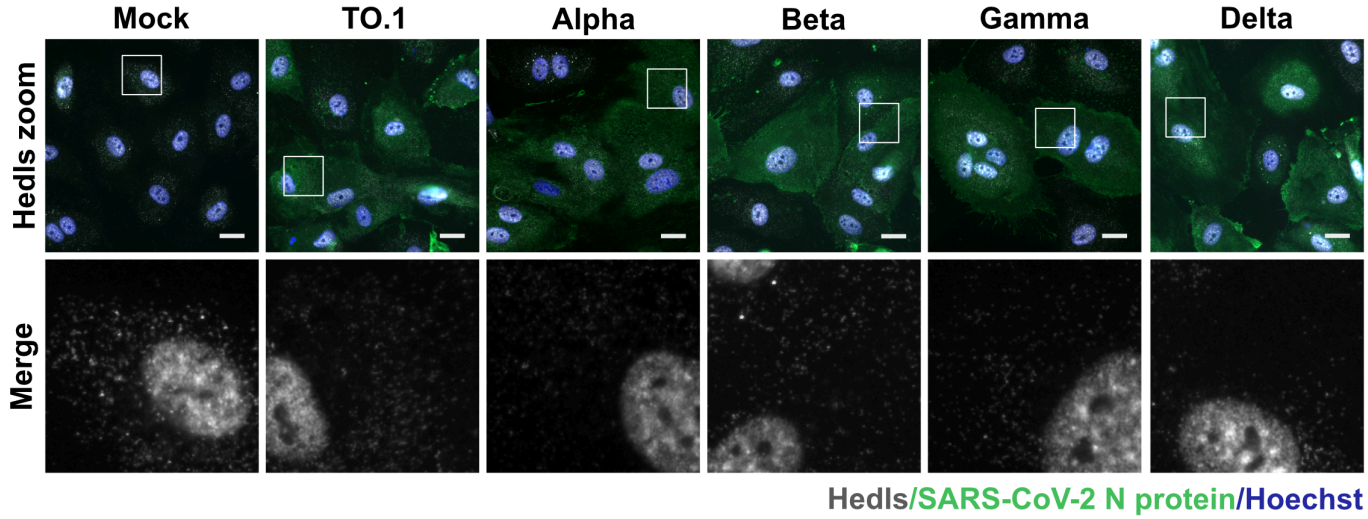
Mock
TO.1
Alpha
Beta
Gamma
Delta
Hedls zoom
Merge
Hedls/SARS-CoV-2 N protein/Hoechst

B

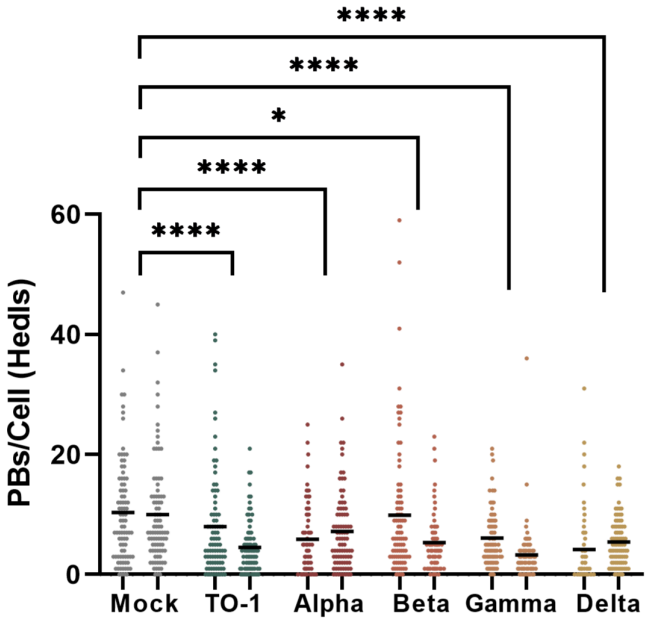
****
****
*
****
****
60
40
20
0
PBs/Cell (Hedls)
Mock
TO-1
Alpha
Beta
Gamma
Delta

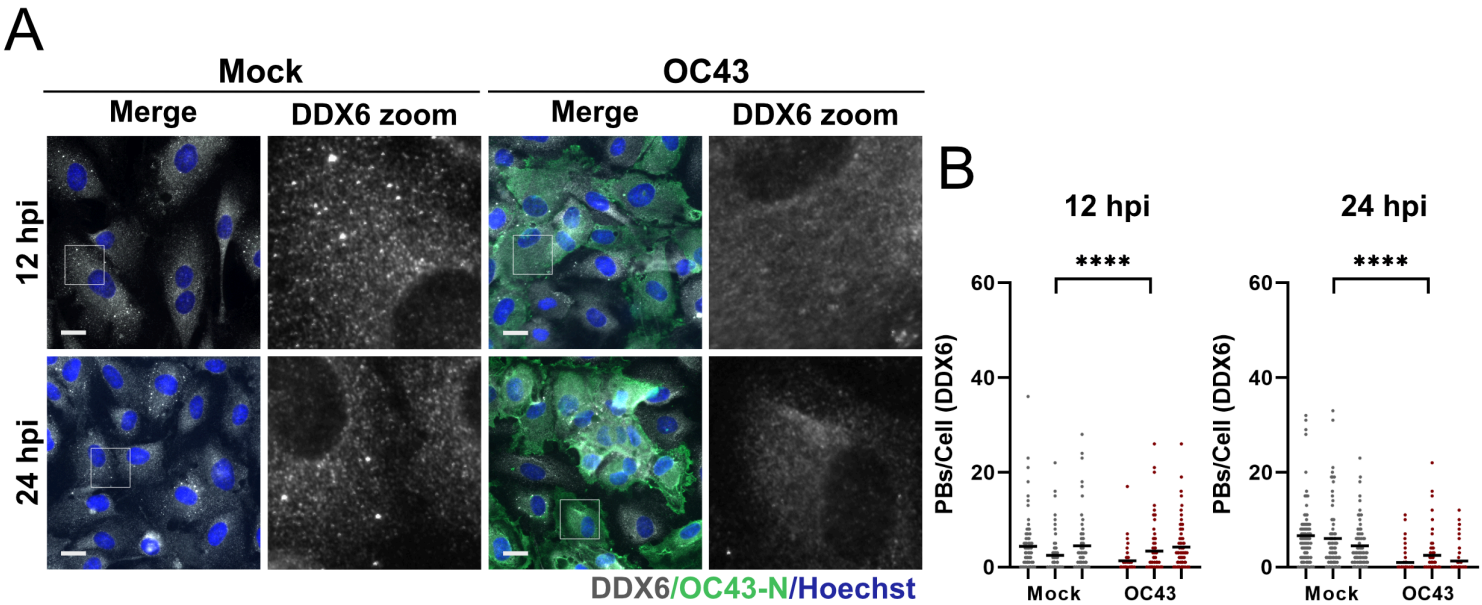
A
Mock
OC43
Merge
DDX6 zoom
Merge
DDX6 zoom
12 hpi
24 hpi
DDX6/OC43-N/Hoechst
B
12 hpi
24 hpi
****
****
PBs/Cell (DDX6)
60
40
20
0
Mock
OC43

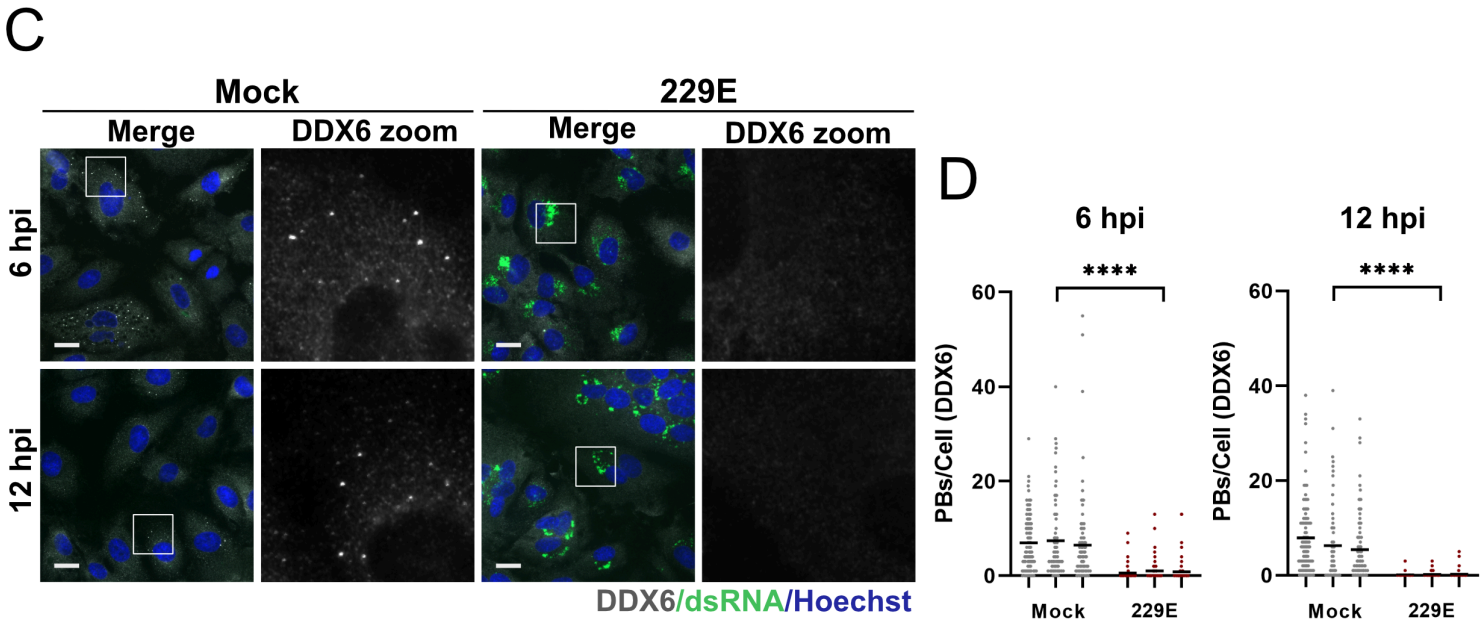
C
Mock
229E
Merge
DDX6 zoom
Merge
DDX6 zoom
6 hpi
12 hpi
DDX6/dsRNA/Hoechst
D
6 hpi
12 hpi
****
****
PBs/Cell (DDX6)
60
40
20
0
Mock
229E

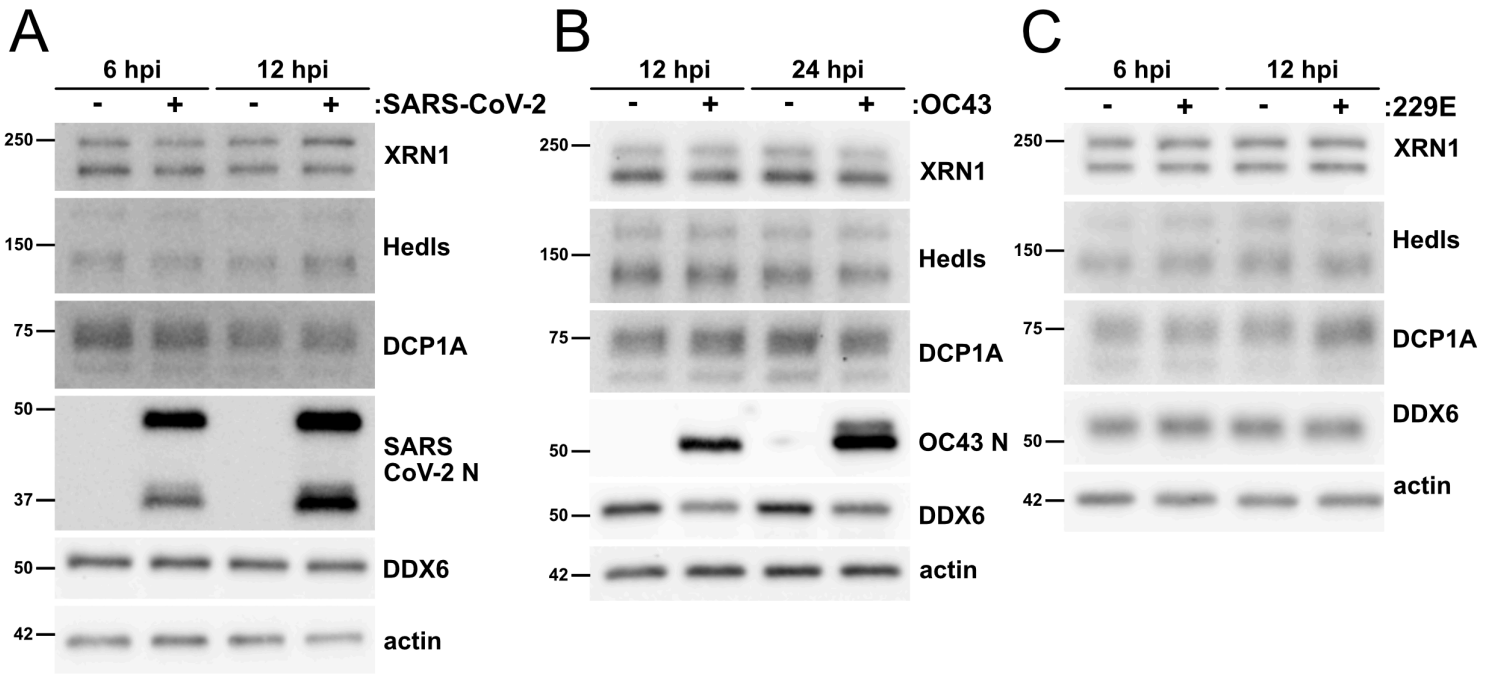
A
6 hpi
12 hpi
- + - + :SARS-CoV-2
250
150
75
50
37
50
42
XRN1
Hedls
DCP1A
SARS CoV-2 N
DDX6
actin
B
12 hpi
24 hpi
- + - + :OC43
250
150
75
50
50
42
XRN1
Hedls
DCP1A
OC43 N
DDX6
actin
C
6 hpi
12 hpi
- + - + :229E
250
150
75
50
42
XRN1
Hedls
DCP1A
DDX6
actin

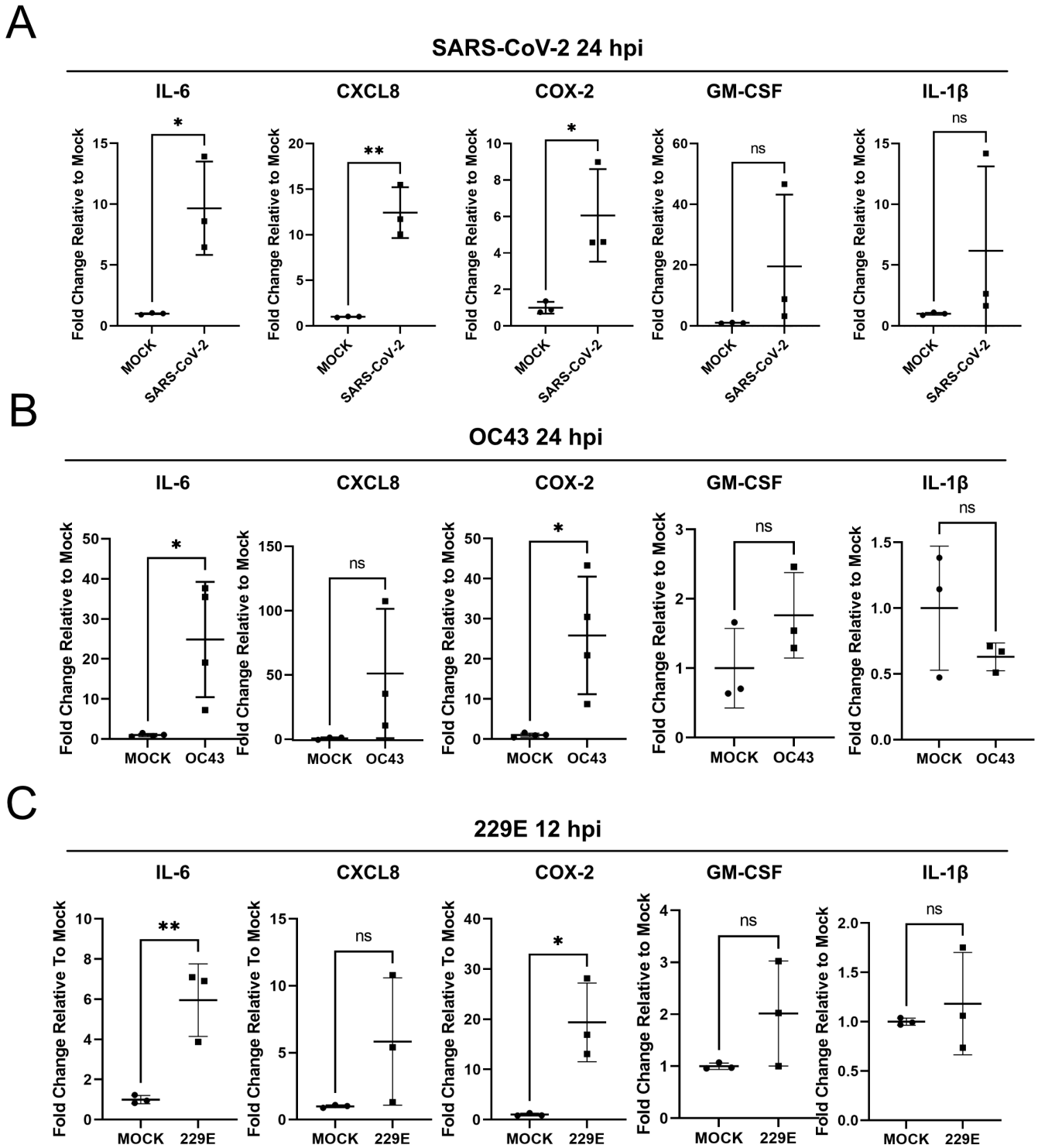
A
SARS-CoV-2 24 hpi
IL-6
CXCL8
COX-2
GM-CSF
IL-1β
Fold Change Relative to Mock
MOCK
SARS-CoV-2
*
**
*
ns
ns
B
OC43 24 hpi
IL-6
CXCL8
COX-2
GM-CSF
IL-1β
Fold Change Relative to Mock
MOCK
OC43
*
ns
*
ns
ns
C
229E 12 hpi
IL-6
CXCL8
COX-2
GM-CSF
IL-1β
Fold Change Relative To Mock
MOCK
229E
**
ns
*
ns
ns

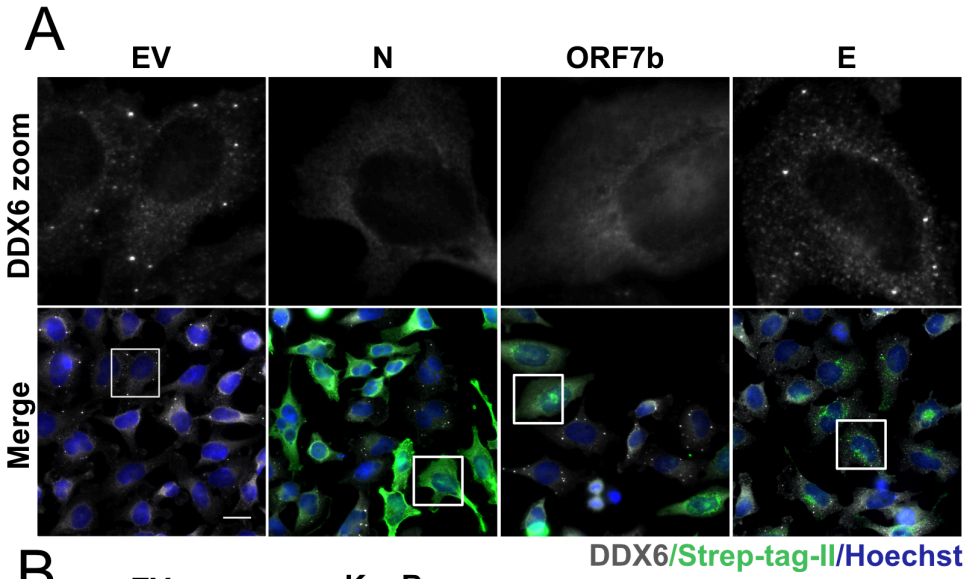
A
EV
N
ORF7b
E
DDX6 zoom
Merge
DDX6/Strep-tag-II/Hoechst

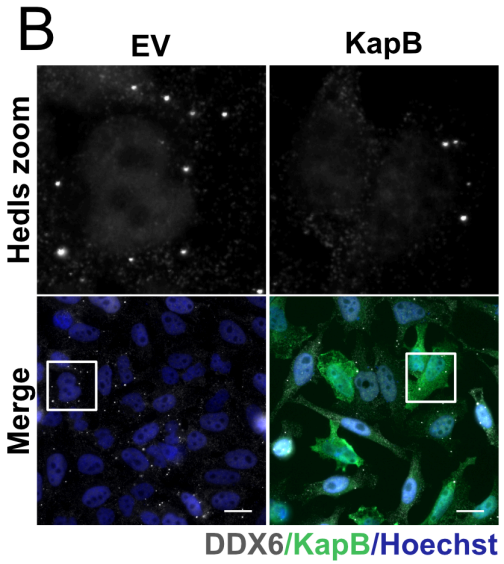
B
EV
KapB
Hedls zoom
Merge
DDX6/KapB/Hoechst

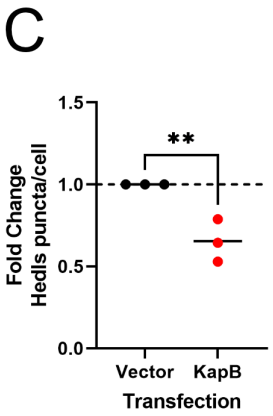
C
Fold Change
Hedls puncta/cell
1.5
1.0
0.5
0.0
**
Vector
KapB
Transfection

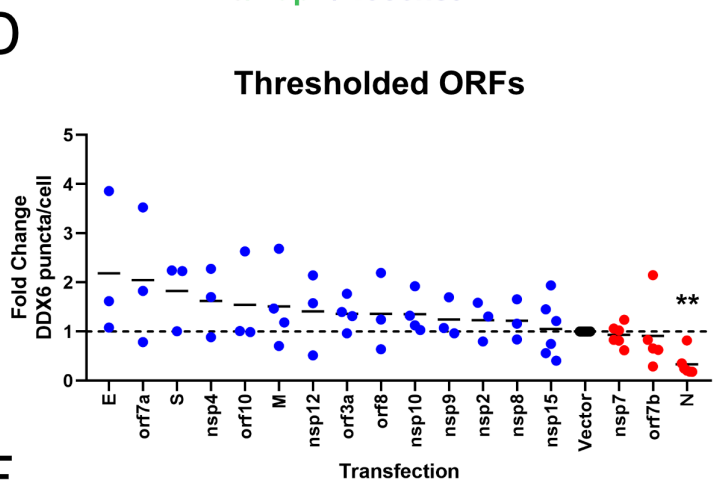
D
Thresholded ORFs
Fold Change
DDX6 puncta/cell
5
4
3
2
1
0
**
E
orf7a
S
nsp4
orf10
M
nsp12
orf3a
orf8
nsp10
nsp9
nsp2
nsp8
nsp15
Vector
nsp7
orf7b
N
Transfection

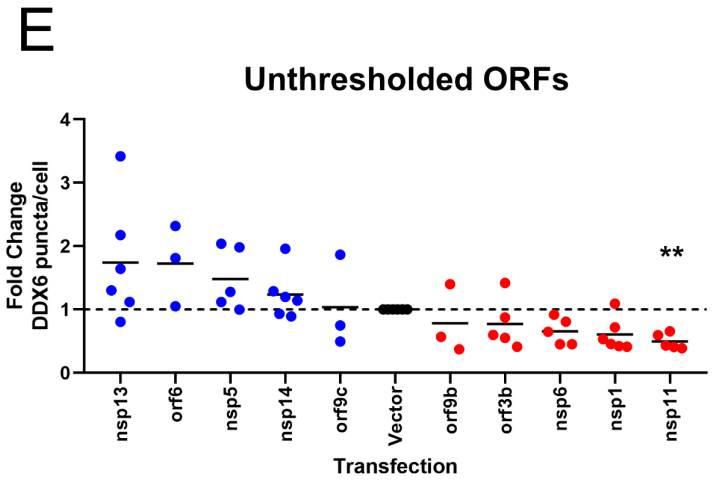
E
Unthresholded ORFs
Fold Change
DDX6 puncta/cell
4
3
2
1
0
**
nsp13
orf6
nsp5
nsp14
orf9c
Vector
orf9b
orf3b
nsp6
nsp1
nsp11
Transfection

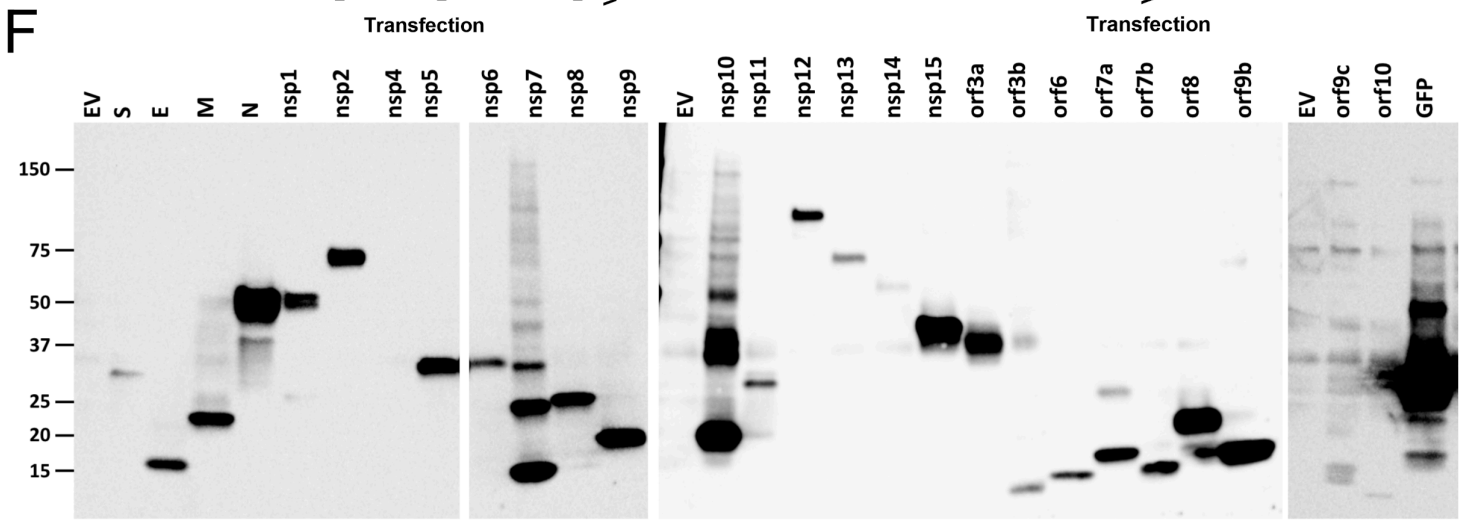
F
EV
S
E
M
N
nsp1
nsp2
nsp4
nsp5
nsp6
nsp7
nsp8
nsp9
EV
nsp10
nsp11
nsp12
nsp13
nsp14
nsp15
orf3a
orf3b
orf6
orf7a
orf7b
orf8
orf9b
EV
orf9c
orf10
GFP
150
75
50
37
25
20
15

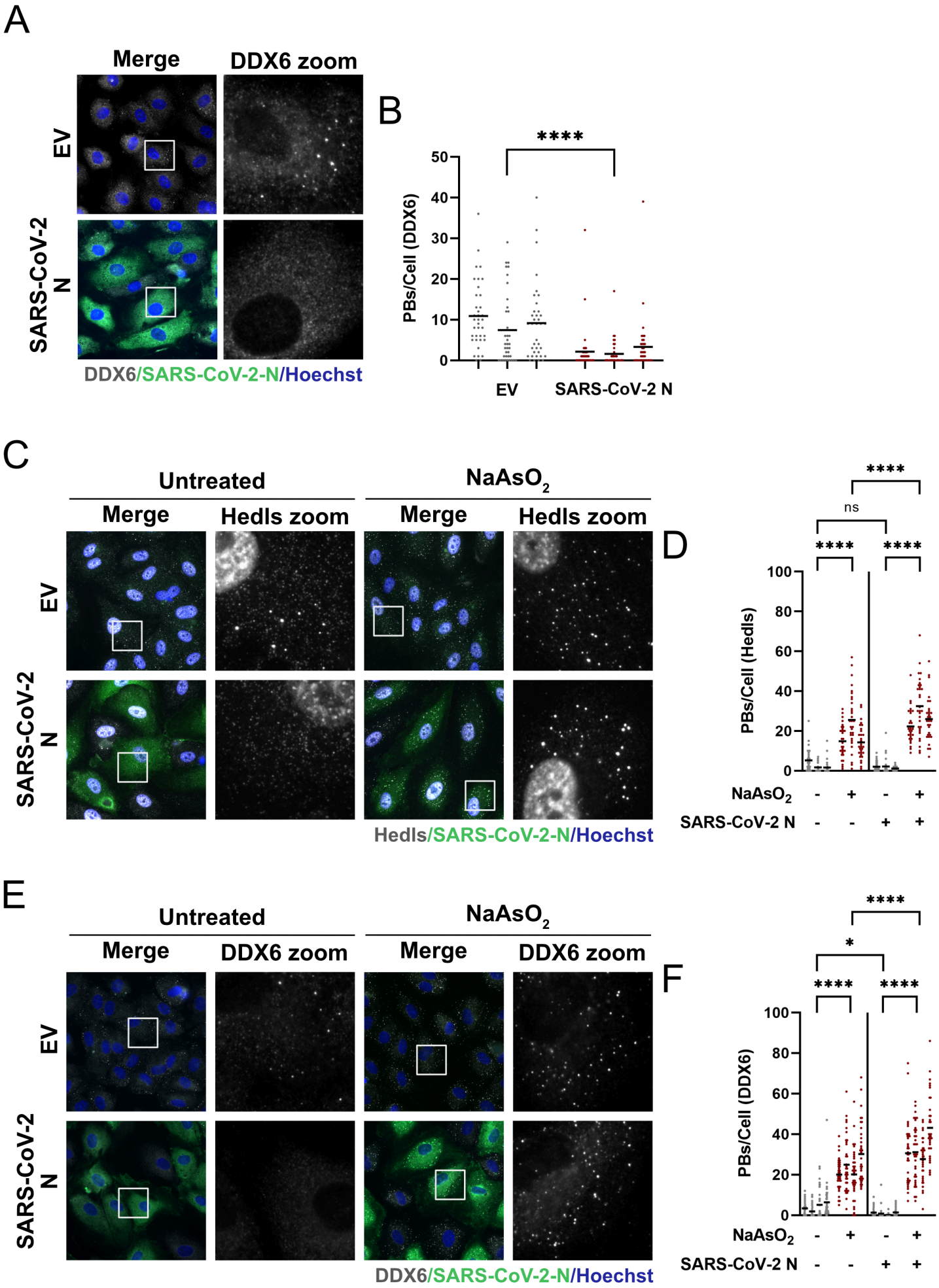
A
Merge
DDX6 zoom
EV
SARS-CoV-2 N
DDX6/SARS-CoV-2-N/Hoechst
B
****
PBs/Cell (DDX6)
50
40
30
20
10
0
EV
SARS-CoV-2 N
C
Untreated
NaAsO2
Merge
Hedls zoom
Merge
Hedls zoom
EV
SARS-CoV-2 N
Hedls/SARS-CoV-2-N/Hoechst
D
****
ns
****
****
PBs/Cell (Hedls)
100
80
60
40
20
0
NaAsO2 - + - +
SARS-CoV-2 N - - + +
E
Untreated
NaAsO2
Merge
DDX6 zoom
Merge
DDX6 zoom
EV
SARS-CoV-2 N
DDX6/SARS-CoV-2-N/Hoechst
F
****
*
****
****
PBs/Cell (DDX6)
100
80
60
40
20
0
NaAsO2 - + - +
SARS-CoV-2 N - - + +

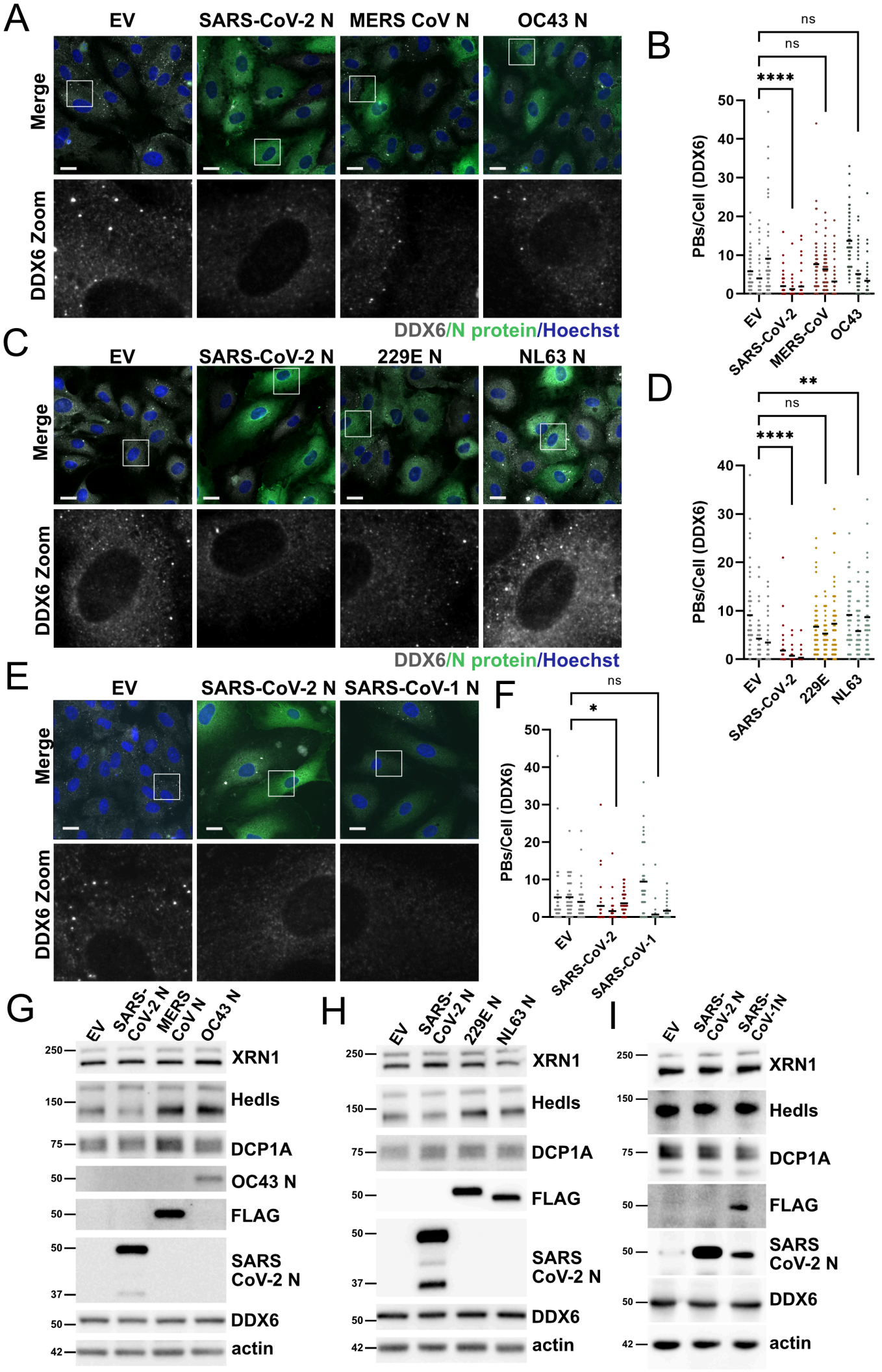
A
EV
SARS-CoV-2 N
MERS CoV N
OC43 N
Merge
DDX6 Zoom
DDX6/N protein/Hoechst
B
ns
ns
****
PBs/Cell (DDX6)
EV
SARS-CoV-2
MERS-CoV
OC43
C
EV
SARS-CoV-2 N
229E N
NL63 N
Merge
DDX6 Zoom
DDX6/N protein/Hoechst
D
**
ns
****
PBs/Cell (DDX6)
EV
SARS-CoV-2
229E
NL63
E
EV
SARS-CoV-2 N
SARS-CoV-1 N
Merge
DDX6 Zoom
F
ns
*
PBs/Cell (DDX6)
EV
SARS-CoV-2
SARS-CoV-1
G
EV
SARS-CoV-2 N
MERS CoV N
OC43 N
XRN1
Hedls
DCP1A
OC43 N
FLAG
SARS CoV-2 N
DDX6
actin
H
EV
SARS-CoV-2 N
229E N
NL63 N
XRN1
Hedls
DCP1A
FLAG
SARS CoV-2 N
DDX6
actin
I
EV
SARS-CoV-2 N
SARS-CoV-1N
XRN1
Hedls
DCP1A
FLAG
SARS CoV-2 N
DDX6
actin

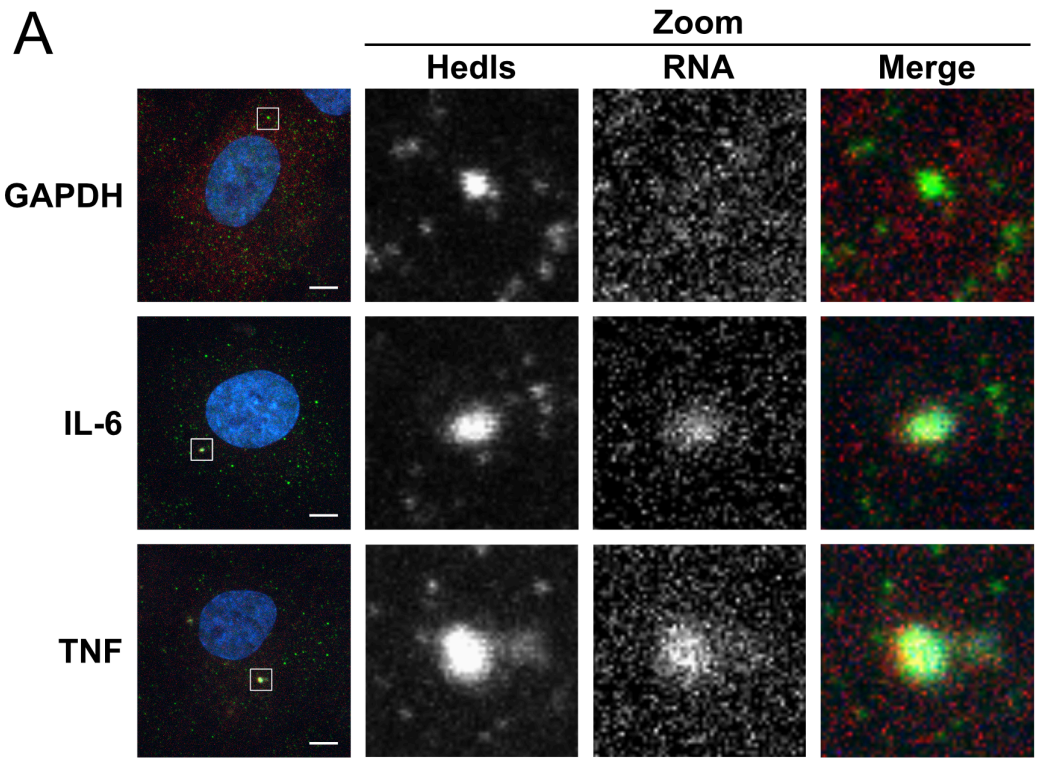
A
Zoom
Hedls
RNA
Merge
GAPDH
IL-6
TNF

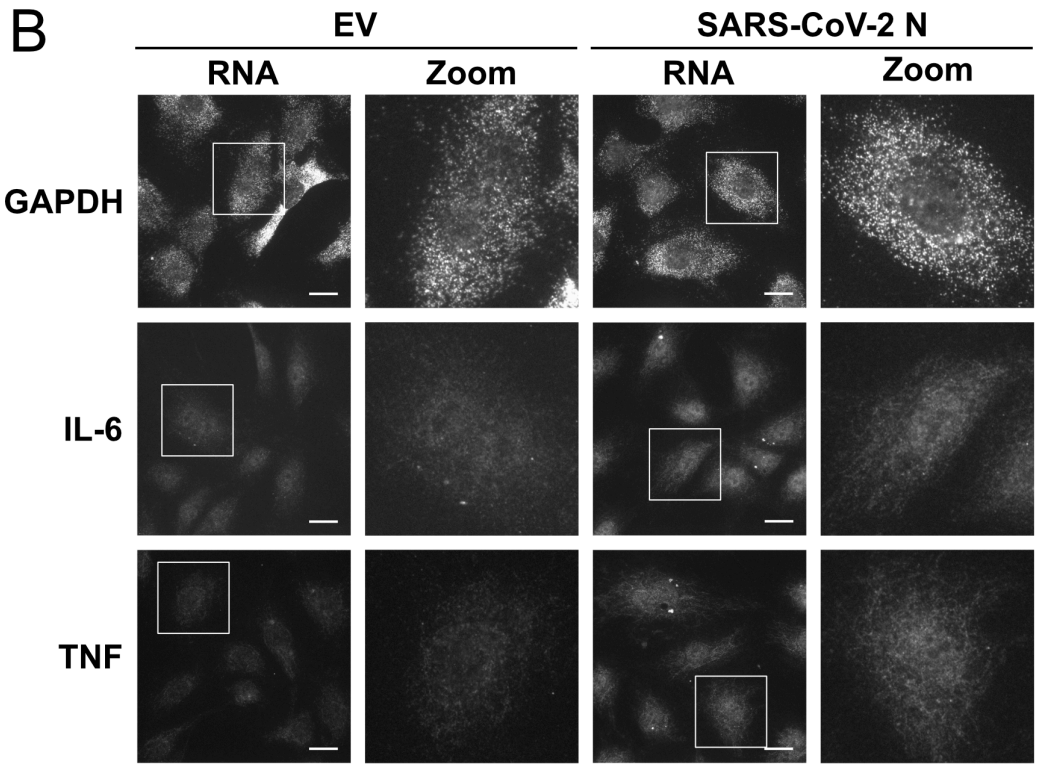
B
EV
SARS-CoV-2 N
RNA
Zoom
RNA
Zoom
GAPDH
IL-6
TNF

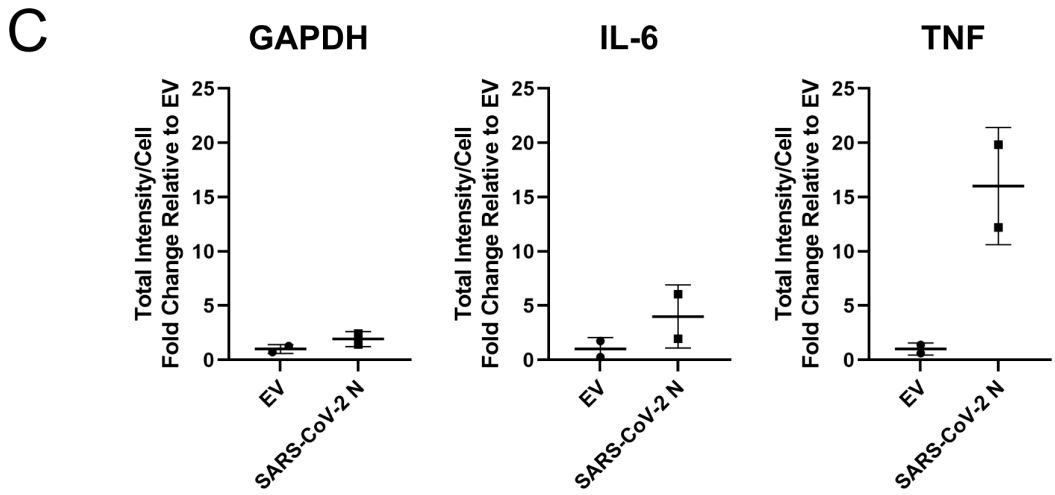
C
GAPDH
IL-6
TNF
Total Intensity/Cell
Fold Change Relative to EV
0
5
10
15
20
25
EV
SARS-CoV-2 N

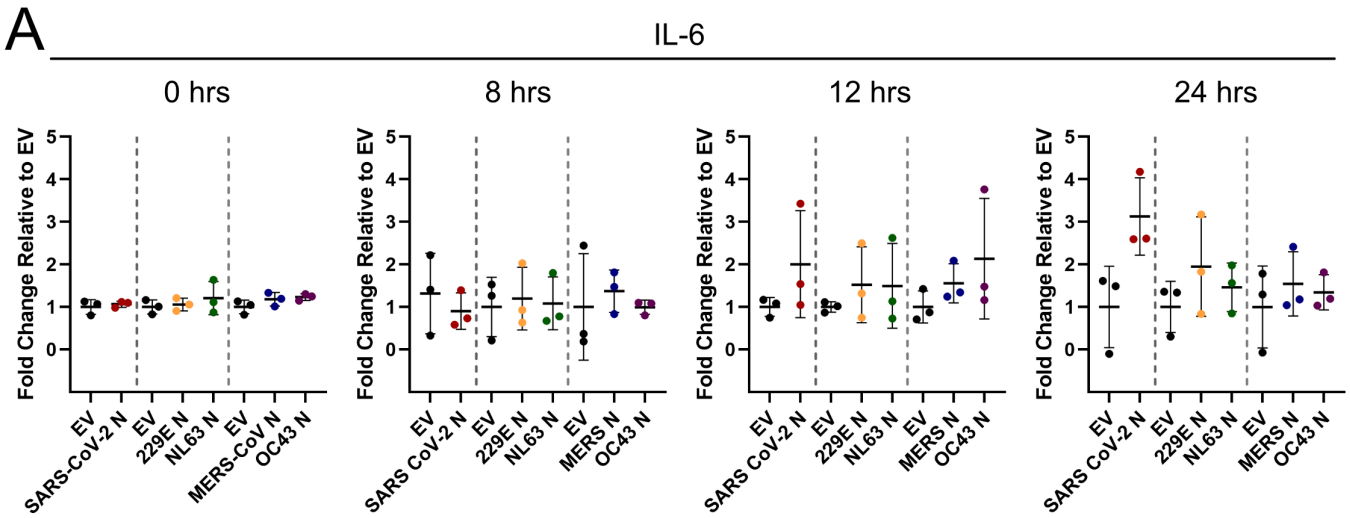
A
IL-6
0 hrs
8 hrs
12 hrs
24 hrs
Fold Change Relative to EV
EV
SARS-CoV-2 N
229E N
NL63 N
MERS-CoV N
OC43 N
SARS CoV-2 N
MERS N

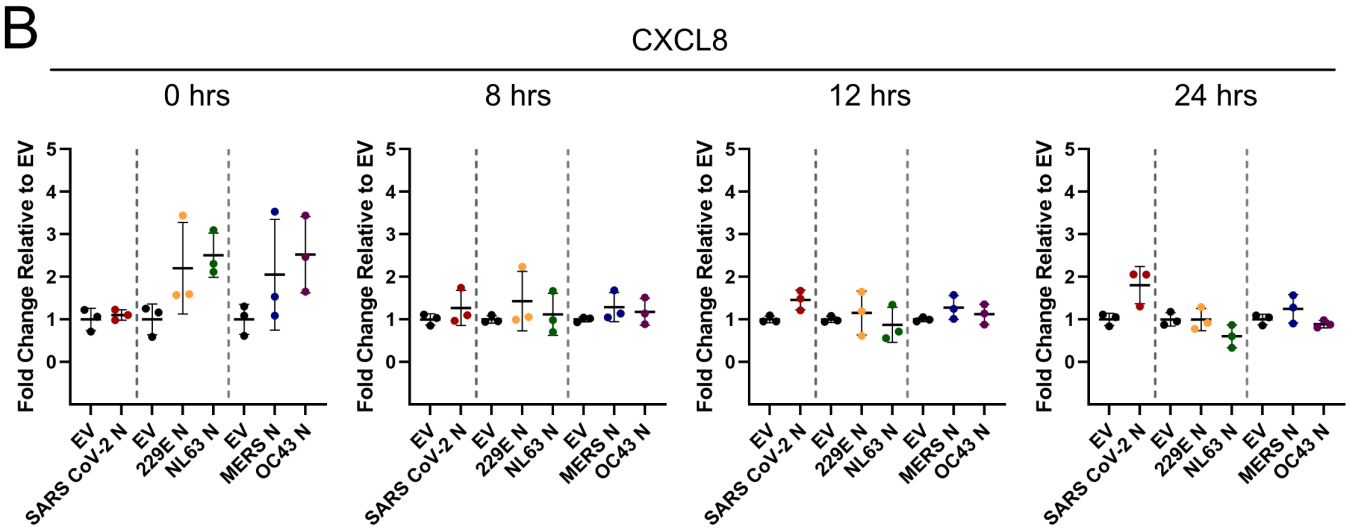
B
CXCL8
0 hrs
8 hrs
12 hrs
24 hrs
Fold Change Relative to EV
EV
SARS CoV-2 N
229E N
NL63 N
MERS N
OC43 N

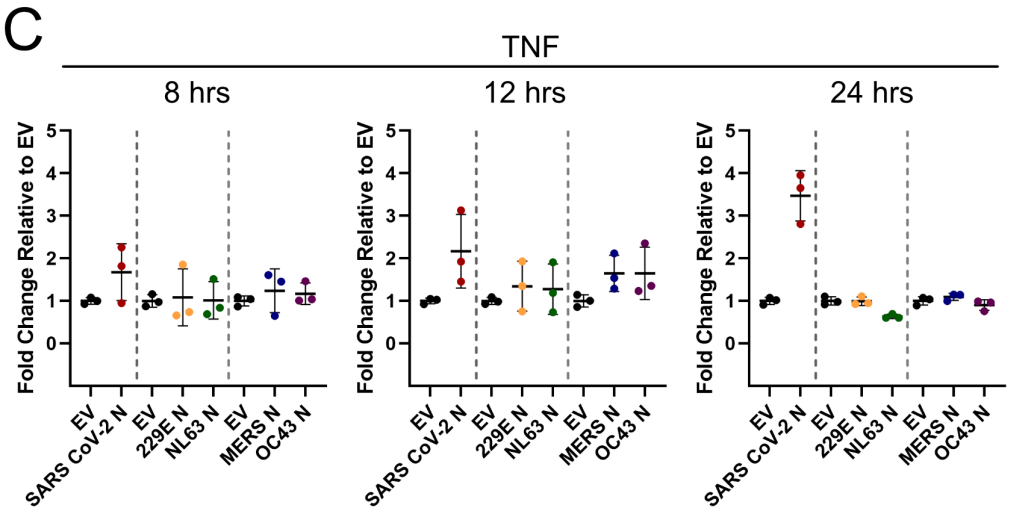
C
TNF
8 hrs
12 hrs
24 hrs
Fold Change Relative to EV
EV
SARS CoV-2 N
229E N
NL63 N
MERS N
OC43 N

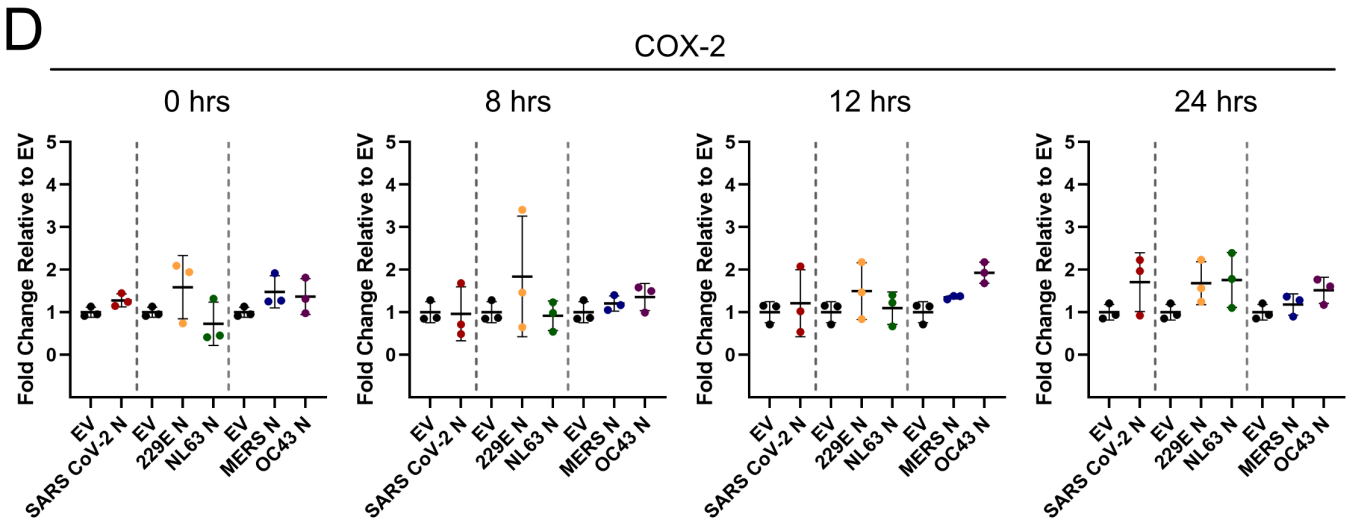
D
COX-2
0 hrs
8 hrs
12 hrs
24 hrs
Fold Change Relative to EV
EV
SARS CoV-2 N
229E N
NL63 N
MERS N
OC43 N